The Astrophysical Journal, 909:150 (20pp), 2021 March 10 https://doi.org/10.3847/1538-4357/abd4e4


# Magellanic Mayhem: Metallicities and Motions

J. Grady, V. Belokurov, and N. W. Evans
Institute of Astronomy, University of Cambridge, Madingley Road, Cambridge, CB3 0HA, UK
*Received 2020 October 20; revised 2020 December 16; accepted 2020 December 16; published 2021 March 12*

## Abstract

We assemble a catalog of Magellanic Cloud red giants from Data Release 2 of the Gaia mission and, utilizing machine-learning methods, obtain photometric metallicity estimates for them. In doing so, we are able to chemically map the entirety of the Magellanic System at once. Our maps reveal a plethora of substructure within our red giant sample, with the Large Magellanic Cloud (LMC) bar and spiral arm being readily apparent. We uncover a curious spiral-like feature in the southern portion of the LMC disk, hosting relatively metal-rich giants and likely a by-product of historic encounters with the Small Magellanic Cloud (SMC). Modeling the LMC as an inclined thin disk, we find a shallow metallicity gradient of $-0.048 \pm 0.001$ dex kpc$^{-1}$ out to $\sim 12^{\circ}$ from the center of the dwarf. We see evidence that the SMC is disrupting, with its outer isodensity contours displaying the S-shape symptomatic of tidal stripping. On studying the proper motions of the SMC giants, we observe a population of them being violently dragged toward the larger Cloud. The perturbed stars predominantly lie in front of the SMC, and we interpret that they exist as a tidal tail of the dwarf, trailing in its motion and undergoing severe disruption from the LMC. We find the metallicity structure in the Magellanic Bridge region to be complex, with evidence for a composite nature in this stellar population, consisting of both LMC and SMC debris.

*Unified Astronomy Thesaurus concepts:* Galaxies (573); Local Group (929); Large Magellanic Cloud (903); Small Magellanic Cloud (1468)

## 1. Introduction

The history of the Large and Small Magellanic Clouds is fraught with complex interactions and, being our nearest example of such a system, provides us with a vital laboratory for detailed study of interacting dwarf irregulars. The Large Magellanic Cloud (LMC) is generally well described by a planar, inclined disk, yet it still displays a host of deviations from this simple picture; it has long been observed to display one dominant spiral arm (see, e.g., de Vaucouleurs 1955; de Vaucouleurs & Freeman 1972) as well as an off-centered stellar bar (e.g., Zhao & Evans 2000; Nikolaev et al. 2004) and shell/ring-like features (e.g., de Vaucouleurs 1955; Irwin 1991; Choi et al. 2018a). In a broad sense, the young stellar populations of the LMC exhibit a clumpy structure, largely congregating centrally around the bar and spiral arm, with little evidence for them residing in the outer regions (see, e.g., Moni Bidin et al. 2017). The LMC interior is host to multiple star-forming regions, most notably 30 Doradus, harboring dense populations of young stellar objects and newly formed stars (see, e.g., De Marchi et al. 2011; Cignoni et al. 2015; Ochsendorf et al. 2017; van Gelder et al. 2020). The recent morphological mapping of the Clouds by El Youssoufi et al. (2019) across a range of stellar ages shows the young main-sequence stars and supergiants of the LMC primarily tracing a fragmented thin bar and spiral-like arms, along with clear over-densities associated with known star-forming regions. On increasing stellar age, red clump (RC) stars and giants are observed to be distributed more smoothly, tracing a thicker bar and diminishing association with the spiral features. Probing the planarity of the LMC using RC stars, Olsen & Salyk (2002) found an inner southwest region to display a prominent warp, curiously located in the portion of the disk nearest to the Small Magellanic Cloud (SMC). More recently, Choi et al. (2018b) identified an outer RC warp in the Cloud, departing from the LMC plane by up to $\sim$4 kpc toward the SMC. Toward the outer regions of the LMC, a plethora of substructure is observed, with Mackey et al. (2016) first identifying a 10 kpc stellar arc located in the northern periphery of the LMC. The optical imaging of the Clouds by Besla et al. (2016) further revealed significant substructure in the northern potions of the LMC. The recent deep imaging of Mackey et al. (2018), in combination with that of the Dark Energy Survey (DES), revealed diffuse stellar substructures residing south of the LMC along with stellar disk truncation in the south and western regions (see also Belokurov & Erkal 2019). Interestingly, toward the northeast of the Cloud, Salem et al. (2015) observed the gas profile of the LMC to be truncated, with no such observation seen in the stellar density profile. They interpreted this to be the result of ram pressure stripping of the LMC gas on its infall through the circumgalactic medium of the Milky Way (MW); such effects have no bearing on the stellar morphology of the galaxy (see also Indu & Subramaniam 2015; Piatti 2018, for a discussion). Belokurov & Erkal (2019) also observed the western stellar truncation of the LMC disk in Gaia giants, employing *N*-body simulations to probe the origin of such a feature from which they concluded that close LMC–SMC passages have the capacity to produce such a one-sided disk deformation.

The state of the metal-poorer SMC is even more complex and disordered, exhibiting a roughly triaxial ellipsoidal shape with substantial depth along various lines of sight (see, e.g., Gardiner & Hawkins 1991; Subramanian & Subramaniam 2012; Deb et al. 2015; Scowcroft et al. 2016; Jacyszyn-Dobrzeniecka et al. 2017; Muraveva et al. 2018). There is evidence of stellar debris tidally stripped by the LMC lying in its eastern regions (Nidever et al. 2013; Subramanian et al. 2017). Centrally, the SMC displays a less prominent bar as well as an eastern wing structure first observed by Shapley (1940), departing from the northern end of the bar toward the LMC. Recent mapping of the SMC by El Youssoufi et al. (2019) has shown the morphology of the younger stellar populations to be highly irregular and largely limited to the SMC bar and eastern

wing, tracing the perturbed gaseous reservoir of the SMC (Stanimirović et al. 2004), with recent star formation expected to have occurred in these regions (see, e.g., Irwin et al. 1990; El Youssoufi et al. 2019). The older stellar populations, on the other hand, display a much more homogeneous spatial distribution (see, e.g., Zaritsky et al. 2000; Haschke et al. 2012; Jacyszyn-Dobrzeniecka et al. 2017) and indeed are offset from the younger populations, as observed by Mackey et al. (2018). Such distinctions are suggestive of historic perturbations to the SMC's gas supply. Furthermore, Olsen et al. (2011) discovered a population of giants residing in the LMC yet distinct in their kinematics with respect to the local field. This disparity was compounded by the fact that these stars were also significantly metal poorer than would be expected for an LMC disk population, leading the authors to the conclusion that these stars in fact originated in the SMC, having been accreted onto the more massive LMC.

The general features outlined above clearly demonstrate that we cannot consider the Clouds independently. Their present-day morphology is directly influenced by historic, mutual interactions, with a striking example being the existence of the Magellanic Bridge (MB). The structure was first observed by Hindman et al. (1963) as a continuous structure of neutral hydrogen linking the two Clouds. Irwin et al. (1985) later discovered this gaseous bridge to be a site of recent star formation. They observed hundreds of blue main-sequence stars to lie in the bridge region, coincident with the H I distribution. The young stellar bridge has also been observed more recently. For example, Casetti-Dinescu et al. (2012) map the bridge with OB stars selected using a combination of UV, optical, and IR photometry. Skowron et al. (2014) utilize OGLE's expansive coverage of the region, while Mackey et al. (2017) trace young stellar associations, ages $\lesssim$30 Myr, from the SMC wing to the outskirts of the LMC, suggesting that their spatial coincidence with the densest regions of H I gas between the Clouds points to these stars having formed in situ. In addition, there is the $\sim$200° long Leading Arm and trailing Magellanic Stream (MS) features associated with the system; purely gaseous in nature, they are strongly indicative of tidal stripping of the Clouds. The simulations of Diaz & Bekki (2012) and Besla et al. (2012) demonstrate that a historic close encounter between the Clouds is able to reproduce the general large-scale features of the MS and Leading Arm. To reproduce the general characteristics of the gaseous MB, a more recent encounter seems to be required, with swathes of gas being stripped from the SMC into the MB region, hosting star formation, alongside stripped stellar debris.

Evidence for a stripped intermediate/old stars in the MB has been seen numerous times (see, e.g., Bagheri et al. 2013; Nidever et al. 2013; Skowron et al. 2014; Carrera et al. 2017). The RR Lyrae (RRL) stars selected from Gaia DR1 by Belokurov et al. (2017) revealed the presence of tidal tails around both the LMC and SMC. They traced a bridge of stars connecting the two Clouds. Studying the 3D structure of this bridge, they found a dual nature; the bridge exhibits one component displaying a smooth distance gradient from the SMC to the LMC, with the other, at the mean distance of the LMC, indicative that the old stellar bridge, is composite in stellar makeup. That is, a large portion of the old stellar bridge is the trailing tail of the SMC, tidally stripped to closer heliocentric distances and toward the LMC. The leading arm is largely compressed on sky and elongated along our line of sight. Belokurov et al. (2017) went on to posit that a significant portion of the bridge is composed of LMC material, tidally dragged into the MB region. The follow-up studies by Mackey et al. (2018) and Belokurov & Erkal (2019) have confirmed the presence of a messy mix of extratidal substructure in this intra-Cloud region, sometimes referred to as "old Magellanic Bridge." Based on Hubble Space Telescope observations, Zivick et al. (2018) showed this close encounter occurred of order 150 Myr ago, with an impact parameter of less than 10 kpc. The extent of the LMC disk is large, with Mackey et al. (2016) observing it to continue to $\sim$18.5 kpc in the DES imaging of the Cloud. Thus, it seems extremely likely that the LMC and SMC have undergone a recent direct collision. The Clouds appear to be on their first infall into the MW (Besla et al. 2007), consistent with the notion that it is LMC–SMC interactions that are the main driver of the substructure we observe. Indeed, the deep photometry from the Survey of the Magellanic Stellar History analyzed by Ruiz-Lara et al. (2020) found evidence for the long-term stability of the LMC's spiral arm, dating its origin to more than 2 Gyr ago and suggesting its independence from the MW interaction.

In this work, we focus on producing metallicity maps of the Magellanic Clouds. These provide a vantage point from which we can observe the complex structural properties of the system. Generally speaking, the LMC is thought to have a shallow negative metallicity gradient through its disk, hosting a metal-rich bar centrally. Cioni (2009) utilized the ratio between C- and M-type asymptotic giant branch stars as an indicator for mean metallicity. Indeed, they detect a metallicity gradient of $-0.047 \pm 0.003$ dex kpc$^{-1}$ in their sample, out to a radius of $\sim$8 kpc from the center of the dwarf. This is consistent with the MC red giant (RG) analysis of Choudhury et al. (2016), whose spectroscopically calibrated photometric [Fe/H] estimates revealed a gradient of $-0.049 \pm 0.002$ dex kpc$^{-1}$ through the LMC disk out to $\sim$4 kpc. They further find evidence for differing metallicity gradients in the northern and southern portions of the LMC disk, in comparison to the eastern and western regions, with the latter being relatively metal poorer. With regards to the SMC, the spectroscopic measurements Carrera et al. (2008) indicated a negative metallicity gradient is also present in the smaller Cloud, with the recent analysis of Choudhury et al. (2020) quoting a gradient value of $-0.031 \pm 0.005$ dex kpc$^{-1}$, derived from their photometric [Fe/H] estimates for SMC RGs. Interestingly, they also saw evidence for asymmetries in the SMC metallicity profile, with it appearing flatter toward the east, in the direction of the LMC, than in the west. They interpret this to be a potential indicator for stellar mixing, acting to flatten the gradient, likely stemming from LMC–SMC interactions. We will assemble a large collection of Magellanic RGs and, on assigning them photometric metallicities through machine-learning methods, map the Magellanic system in its entirety and explore the structures that lie therein.

## 2. Data

We make use of the Magellanic RG catalog compiled by Belokurov & Erkal (2019) from Data Release 2 (Gaia Collaboration et al. 2018b) of the Gaia mission (Gaia Collaboration et al. 2016), which holds 1,604,018 stars within 30° of the Clouds. In the top row of Figure 1, we show the stellar density of these giants in two coordinate systems: the MS system ($L$, $B$) described by Nidever et al. (2008) and the

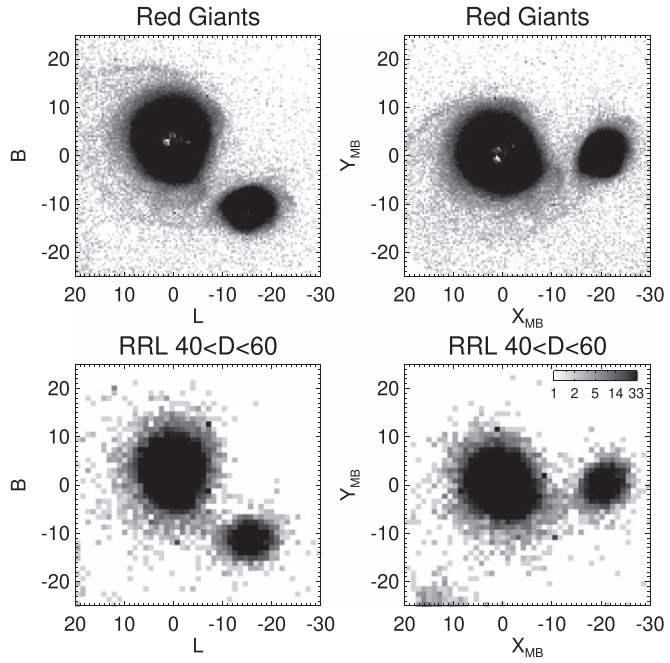


**Figure 1.** The top two panels show the red giant sample of Belokurov & Erkal (2019) shown in both Magellanic Stream and Magellanic Bridge coordinates. A myriad of diffuse stellar substructure can be seen in the outer regions of the system. Most prominent is the northern spiral-like feature that was first observed by Mackey et al. (2016), alongside a host of complex thin streams in the southern portions of the outer LMC. The bottom two panels display Gaia DR2 RR Lyrae, whose selection we describe in the text. Note that the RR Lyrae distribution follows closely that of the giants, including the sharp cutoff in the disk density on the side of the LMC facing the SMC. With both stellar tracers, the old stellar bridge (Belokurov et al. 2017) is evident as the connecting feature of the two Clouds.

MB system as in Belokurov et al. (2017), both of which will be utilized in this work. A plethora of substructure is seen in the giants, with the Clouds hosting multiple outer spiral-like arms such as the northern structure identified by Mackey et al. (2016). A complex ensemble of features are present in the southern portion of the LMC; the claw-like features, associated with "Substructure 1" and "Substructure 2" of Mackey et al. (2018), appear to wrap clockwise around the lower LMC disk. As noted in Belokurov & Erkal (2019), one of the most striking features is the thin stellar stream that appears connected to the SMC, arcing $\sim 90^{\circ}$ clockwise around the outer LMC. Curiously, hints of this structure may already be seen in the map of the Magellanic Mira built using Gaia DR1 data in combination with WISE and 2MASS photometry (Deason et al. 2017). The portion of the LMC disk nearest the SMC is truncated, with the morphology of the smaller dwarf appearing distorted, apparently stretching toward the LMC. The outskirts of the two galaxies are littered with stellar debris, and indeed, a population of giants is observed to inhabit regions between the Clouds. In the lower two panels of the figure, we show, for comparison, the distribution of RRL in the two coordinate systems, combining both the Gaia SOS (Specific Object Study; Clementini et al. 2019) catalog with stars classified as RRL in the general variability table `vari_classifier_result` (Holl et al. 2018). Requiring these RRL to have `phot_bp_rp_excess_factor` $< 3$, we correct for extinction and assign heliocentric distances as in Iorio & Belokurov (2019). Selecting those RRL whose distances are commensurate with the Clouds, we see in Figure 1 that a relatively clean selection can be made. The peripheries of the dwarfs are again scattered with diffuse structures, the LMC disk is truncated toward the SMC and most striking of all is the old stellar bridge spanning in the inter-Cloud region. Interestingly, the RRL distribution follows closely that of the giants, implying that in the LMC, many of these old pulsating stars represent the disk population. This is perhaps best reflected by the sharp disk truncation on the side nearest to the SMC. Both RGs and RRL show this dramatic near-linear cutoff in the disk density. The evacuated western portion of the LMC's disk emphasizes strikingly the old bridge connection between the two Clouds.

We cross-match the Magellanic giant sample in the 2MASS (Skrutskie et al. 2006) and WISE (Wright et al. 2010) surveys to build a sample with broad photometric coverage. We only select stars with the 2MASS quality flags `ph_qual` = AAA, `cc_flg` = 000, `gal_contam` = 0 and the WISE quality flags `ext_flg` $\leqslant 1$, `ph_qual` = AAA to remove potential artifacts and sources with poor photometric measurements. Initially, we correct for extinction using the dust maps of Schlegel et al. (1998) and the 2MASS and WISE extinction coefficients of Yuan et al. (2013). For the Gaia photometry, we follow the dereddening procedure of Gaia Collaboration et al. (2018a), using the first two terms in their Equation (1) to do so. The recent red clump calibration of Skowron et al. (2021) has provided reddening maps for the LMC and SMC with good resolution in the central parts of the Clouds, regions where those of Schlegel et al. (1998) suffer from high levels of dust. Consequently, we utilize these recent maps for the innermost regions of the Clouds.[1] We then require the giants to obey the relation of `phot_bp_rp_excess_factor` $< 1.3 + 0.06$ (`BP_RP`)$^2$ and reject any stars that now lie outside the color–magnitude diagram (CMD) selection box of Belokurov & Erkal (2019), after correcting the extinctions in the inner regions, yielding a sample size of 226,119 Magellanic giants.

A subset of our sample is captured by the APOGEE-2 southern hemisphere observations (Majewski et al. 2016; Zasowski et al. 2017), the MC targets of which provide a relatively unbiased sample of stars spanning a large metallicity range of [Fe/H] $= -0.2$ dex down to [Fe/H] $= -2.5$ dex (see Nidever et al. 2020). This provides us with metallicity values for 3077 giants. Figure 2 shows the spatial distribution of our giant sample, with red markers indicating those stars with APOGEE measurements. Our full sample spans the entirety of the Magellanic region, with the APOGEE stars also exhibiting good spatial coverage of the Clouds in both the radial and azimuthal sense. We will utilize this subsample as a training set to build a regression model that can accurately predict the metallicities for our full giant sample. In Figure 3, we show the CMDs of our giants with the extent of the training APOGEE data indicated by the black contours. The WISE and 2MASS CMDs are relatively clean with clearly discernible RG branches (RGB) and asymptotic giant branches (AGB) seen; the marked drop in stellar density at approximately $K_s < 12$ and W1 $< 12$ marks the transition to the AGB stellar populations of which our sample encompasses both the oxygen-rich (O-rich) and carbon-rich (C-rich) components of this phase. The stars for which APOGEE measurements exist are largely confined to bright RGs, with a noticeable lack of stars bluer than $\sim -0.2$ in the WISE color W1 $-$ W2 in comparison to the full sample. The effects that such color offsets have on our ability to

[1] We also applied this procedure to the RRL in Figure 1.

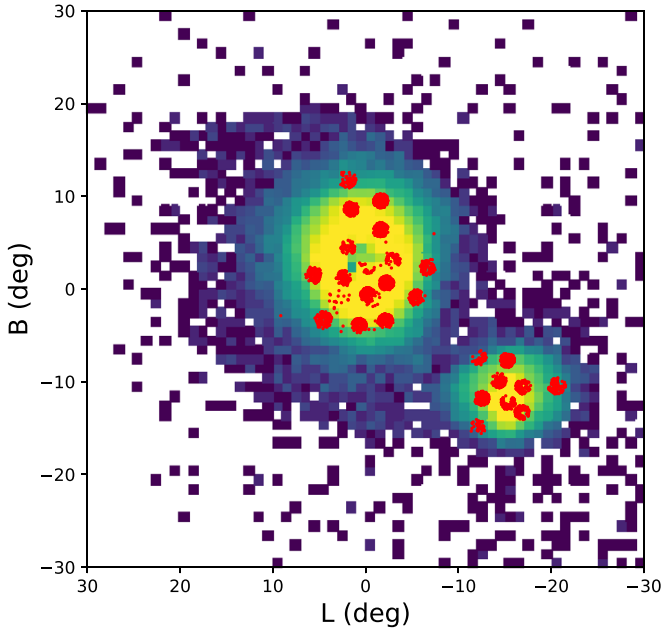


**Figure 2.** Spatial distribution of our giants in Magellanic Stream coordinates. Stars with an APOGEE spectroscopic metallicity measurement are shown in red and provide good coverage of both satellites. These stars will constitute our regression training set to predict the metallicities of all the Magellanic giants in our sample.

accurately predict metallicities are discussed later in this paper. APOGEE DR16 has observed ∼23,000 stars in the direction of the Magellanic Clouds, largely comprising RGB, AGB, and foreground dwarf stars (Zasowski et al. 2017). Recently, Nidever et al. (2020) selected Magellanic giants from APOGEE by utilizing optical photometry to remove foreground dwarfs and devised a 2MASS photometric selection to isolate likely Magellanic giants. The authors acted to ensure there was minimal bias against selecting metal-poor giants by employing a wide range in $(J - K_s)$ selection. We probed our APOGEE sample in relation to that of Nidever et al. (2020) by selecting all APOGEE+Gaia+2MASS+WISE stars within 40° of the LMC as a comparison sample. We then applied our photometric cleaning cuts outlined earlier in this section, as well as requiring parallax values to be less than 0.2, and employed a proper motion cut similar to that in Belokurov et al. (2017). We did not implement the CMD selection of Belokurov et al. (2017) but rather selected stars in the $(J - K_s)$ versus $H$ Magellanic Cloud RG selection box of Nidever et al. (2020). We then assessed the level of bias that our Gaia CMD giant selection incurs against giant metallicity by assessing our sample completeness with respect to this comparison sample. In doing so, we estimate our sample completeness to be ∼80%–90% across our full metallicity range and conclude that no significant bias against any particular metallicity is present in the data we will use to build our regression model.

## 3. Regression Analysis

Through a process of experimentation, we choose a feature vector of $\boldsymbol{f} = [BP–RP, RP–H, \mathrm{W1–W2}, J–H, J–K_s]$ to utilize in predicting photometric metallicities. The top row of Figure 4 shows the distribution of the APOGEE training set across five CMDs. We assess the photometric correlation with metallicity in the middle row of the figure, where across the feature vector we see clear metallicity gradients in the CMDs, especially so in the WISE photometry owing to its near-vertical RGB. Computing the pair-wise correlations between training set features and metallicities yields the correlation vector [0.33, 0.45, −0.65, 0.46, 0.47], where elements are ordered in correspondence with the feature vector $\boldsymbol{f}$. These correlations are shown explicitly in the bottom row, where we see the strong correlation of the WISE color with metallicity. The WISE W2 band covers the CO molecular absorption feature that is strongly dependent on stellar metallicity. Metal-rich giants are bright in the W1 band only whereas metal-poor giants are bright in both W1 and W2. Consequently, stars that are blue in W1 − W2 are in fact metal richer, as seen in Figure 4 (see, e.g., Schlaufman & Casey 2014; Koposov et al. 2015; Casey et al. 2018). The Gaia features $BP - RP$ and $RP - H$ are included as both bear strong correlations with effective temperature, which itself affects the photometric color of stars. We first set aside 30% of our Gaia+APOGEE+2MASS+WISE sample as a test set, unseen by the learning algorithm throughout the training process and used for a final evaluation of the model's performance. Utilizing the Support Vector Regression (SVR) implementation of `scikit-learn` (Pedregosa et al. 2011), we implement a standard radial basis function kernel of the form

$$K(\boldsymbol{x}_1, \boldsymbol{x}_2) = \exp\left(-\gamma\,|\boldsymbol{x}_1 - \boldsymbol{x}_2|^2\right) \quad (1)$$

and optimize the algorithm's parameters, namely, $\gamma$ and regularization parameter $C$, through a $K$-fold cross-validation grid search, with 10 splits, accepting parameter values that minimize the rms error (RMSE). We choose to use an SVR algorithm as it has the ability to model complex, nonlinear relations between the features with relatively few parameters to tune. The performance of the regressor is first assessed through the learning curve shown in Figure 5 where the learning algorithm is trained on an incrementally increasing number of training points. A validation sample is set aside beforehand, from which we can evaluate the performance of the model with respect to our chosen metric (RMSE) at each incremental step. The general trend of the figure shows both curves tending toward a final RMSE of ∼−0.16 dex, an acceptably low value that validates the algorithm to be sufficiently unbiased. The convergence of the two curves also indicates relatively low variance—a regressor suffering from overfitting would yield curves that tend toward convergence but still remain offset by a significant value even when maximal training data are available.

### 3.1. Regression Performance

The upper-middle panel of Figure 6 shows good one-to-one agreement between the APOGEE spectroscopic [Fe/H] values and those predicted by our trained regressor. The upper-right panel of the figure shows we are able to reasonably reproduce the metallicity distribution of the test data. The lower panels of the figure show the mean squared error (MSE), squared bias, and variance as a function of APOGEE metallicity for the predictions on our test set. The model suffers from relatively little bias across the full metallicity range, with most contribution occurring at [Fe/H] $< -1.25$ dex. Generally, the main contribution to the total error stems from variance in the predictions. This is particularly the case at the low-metallicity end where data are sparse, leading the model to overfit in this region. The predictions are biased high by ∼0.15 dex for

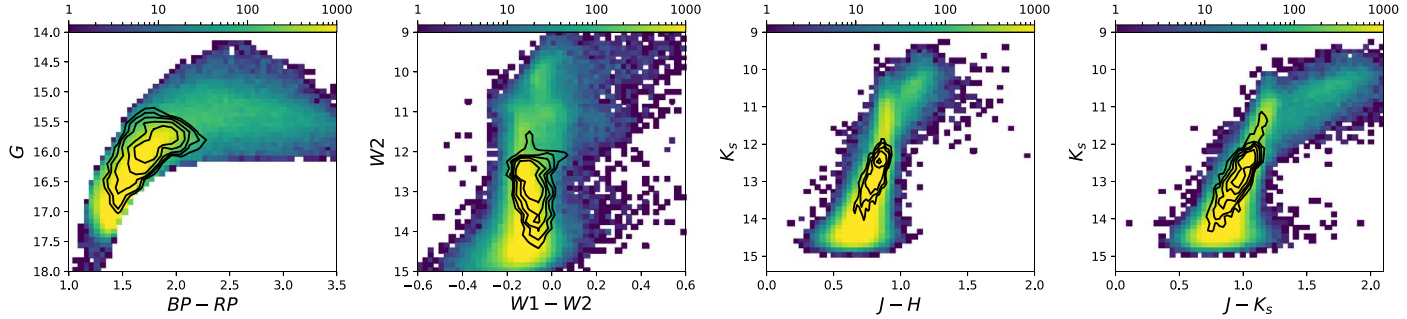


**Figure 3.** CMD diagrams of the full Gaia+2MASS+WISE giants for which we will predict metallicities. We see our giant sample encompasses the upper RGB out to the AGB stellar phase. The cleanliness of the Gaia CMD is a direct consequence of the methods employed by Belokurov & Erkal (2019) in their giant selection. In the other photometric systems, the CMDs look relatively clean, and we overlay black contours spanning the 5th–50th percentile levels of the APOGEE training sample, with logarithmic spacing. It can be seen that APOGEE generally obtains metallicity estimates for the brighter red giants, with the sample being particularly deficient in blue WISE colors. How this pertains to our regression analysis is discussed later in this work.

metallicities less than −1.5 dex and are biased slightly low by ∼0.1 dex at the most metal-rich end. For metallicities less than −1.2 dex, the RMSE is approximately 0.2 dex and the RMSE across all metallicity values is 0.15 dex. We list our prediction errors in four metallicity bins in Table 1. We stress that these are purely nominal error estimates and likely underestimated in some cases. We also note that these nominal errors we obtain from our test set analysis will naturally contain uncertainty invoked from the age–metallicity degeneracy, an effect that acts to make younger/older stars bluer/redder and hence our model would predict these stars to be more metal-poor/-rich than they actually are.

### 3.2. Regression Predictions

We use our trained SVR to predict metallicities of our full Gaia+2MASS+WISE giants, whose spatial distribution is shown in Figure 2. We consider the fact that our full giant sample encompasses a much wider color range than that of our APOGEE subset, particularly so for W1 − W2 as seen in the comparison of Figure 3 with Figure 4. To account for this, we adopt a nearest neighbor approach, computing the mean Euclidean distance in feature space from each of our giants to those in the APOGEE subset using five nearest neighbors. We can then choose an appropriate upper-limit cut on this mean feature distance, $\langle D_{NN} \rangle$, to reject stars whose photometry is not well represented in the training data. We also impose cuts in the 2MASS colors for which we require $J - H < 1$ and $J - K < 1.25$. In effect, this selection rejects the very red, likely C-rich, AGB stars from our sample. Such extremely red stars are poorly represented in the APOGEE training data and so the regression model will likely struggle to accurately interpolate values to this regime. We also further investigate the effect of removing the AGB branch by only considering stars with $K_s > 12$ (this selection is tuned to the LMC AGB as it is the dominant contributor to our sample). The effects of these individual selections are shown in Figure 7, which shows the predicted metallicity as a function W1 − W2 color for our Gaia +2MASS+WISE giants. The leftmost panel clearly shows spurious predictions accumulating at [Fe/H] ∼ −1 dex, toward red values of W1 − W2. On applying our 2MASS color cuts, we eliminate these entirely, as we cull the extremely RGs from our sample. The selection of stars fainter than $K_s > 12$ highlights the region occupied by likely AGB stars which consists of a spur branching out from the main color–metallicity relation, an effect caused by the WISE AGB isochrone tracks turning red and crossing the RGB track at other fixed metallicities (see Figure 1 of Koposov et al. 2015). The rightmost panels in the figure show the effect of requiring the nearest neighbor mean feature space distance $\langle D_{NN} \rangle$ to be less than 0.06, corresponding to a cull of stars within the largest 10th percentile. This selection acts to remove stars whose photometric colors deviate largely from the regime spanned by our APOGEE sample, thus eliminating spurious extrapolations in our metallicity estimates. This is evident from the panel, where stars extremely blue in W1 − W2, and whose predicted metallicities spuriously converge to ∼−0.8 dex, are effectively removed. The bottom panels of the figure show our predicted metallicity distribution function (MDF) in each of the cases. Aside from the most spurious defections, these distributions behave well with both the LMC and SMC exhibiting appearing negatively skewed with long tails toward the metal-poor end. Hereafter, we will only consider giants in our analysis whose 2MASS colors obey they cuts $J - H < 1$ and $J - K < 1.25$, as it is this selection that eliminates the most serious artifacts in our predictions, yielding a sample of 218,077 giants. We will note explicitly in the text when we apply further cleaning criteria to our giant sample. Considering stars within a 12° aperture of the LMC, we obtain a median metallicity value of −0.78 dex, with the peak of the (skewed) distribution occurring at ∼−0.67 dex. For stars falling within a 6° aperture of the SMC, we obtain a median metallicity value of −0.96 dex, with the distribution peaking at ∼−0.93 dex.

## 4. Metallicity Maps

We show the mean predicted metallicity across the Clouds in the left panel of Figure 8, using the MS coordinate system of ($L$, $B$). The LMC bar is strikingly clear as a central metal-rich structure in our giant sample. Outside of the bar region, diffuse arcs and spiral arm-like structures are seen both in the northern and southern portions of the LMC disk. We note that the structures apparent in this figure, and to be discussed later in this work, are viewed in projection and any reference to them will be done so with this in mind, unless otherwise stated. The LMC metallicity profile then decays into the outskirts, where it is littered with more metal-poor stars. The SMC giants are seen to be predominantly metal poor, with only the most central region showing enhancement. The majority of substructure in the outskirts of the Clouds also appears to be relatively metal poor, with the northern stream-like substructure, identified first by Mackey et al. (2016), apparent in our sample. The Clouds

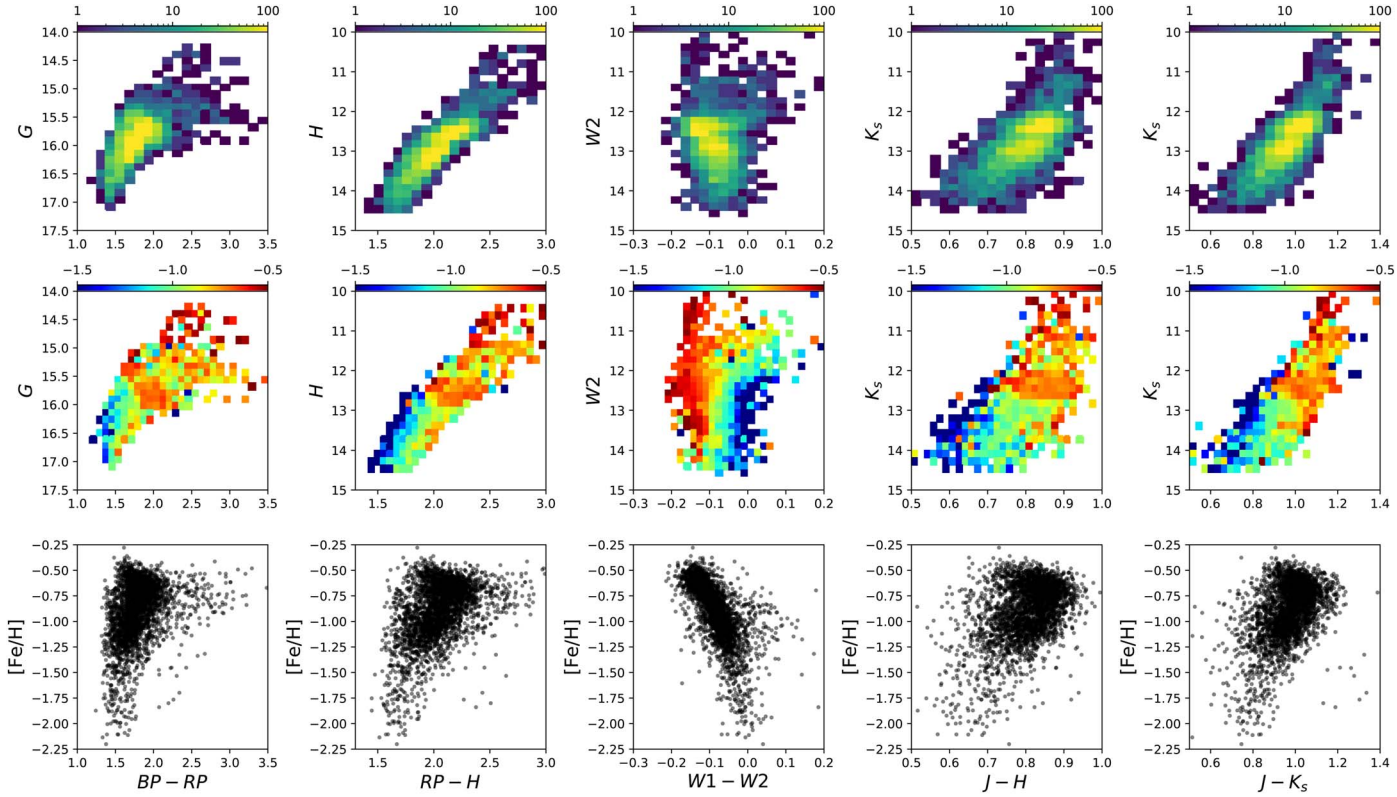


**Figure 4.** Top row: CMD of our APOGEE training set across the Gaia, 2MASS, and WISE photometric systems utilized in this work along with the addition of the Gaia+2MASS combination chosen as a feature in our regression analysis. The bulk of the stars lie in the upper RGB with few AGB stars present. Middle row: the color scheme here shows the mean metallicity in each pixel. Gradients are clear across all colors, especially so in WISE owing to its near-vertical RGB. Bottom row: scatter plots between each of our four chosen features and APOGEE metallicity are shown. Positive correlations are evident with the WISE band showing the tightest relation.

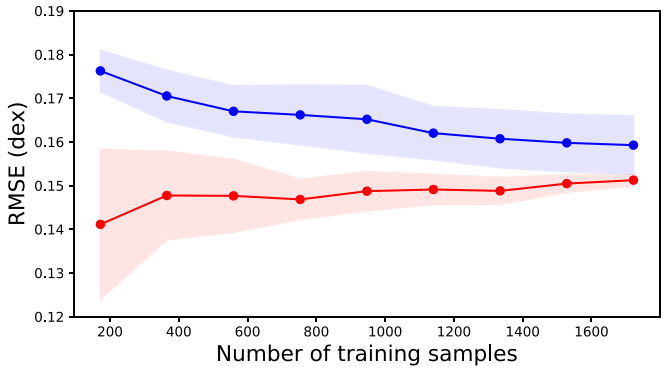


**Figure 5.** Learning curves for an SVR trained using a feature vector of [*BP*–*RP*, *RP*–*H*, W1–W2, *J*–*H*, *J*–*K*]. A cross-validation set is separated out and the algorithm is trained on incrementally increasing training set size. The rms error (RMSE) score is then computed at each stage for both the training and validation set. Both curves tend toward each other smoothly to a sufficient accuracy of ∼0.17 dex. The good convergence and low final accuracy indicate the learning scenario has sufficiently low bias and variance.

appear to be connected, largely with metal-poor stars, in two regions: that of the MB consisting of stars likely stripped from the SMC and dragged toward the LMC, as indicated by the proper motion analysis of Schmidt et al. (2020), and also in a region south of this at $L \sim 8°$, at the end of a narrow tail-like substructure that wraps around the eastern edge of the LMC (see Figure 2 herein and Figure 2 of Belokurov & Erkal 2019 also). Denoting the $i$th percentile of the LMC/SMC MDF as $p_i$, we show in the middle panel the difference of $p_{90} - p_{10}$, which represents the width of the distribution. The central regions of the LMC display a consistently narrow MDF with that of the SMC generally quite broad, likely a projection effect of its extensive line-of-sight depth. In the right panel, we show the ratio of $(p_{95} - p_{50})/(p_{50} - p_5)$, which provides a sense of the direction of skew that the MDF possesses. The most central regions of the LMC show values close to unity, i.e., nearly symmetric, as metal-rich stars dominate in this region and counteract the inherent left skew of the MDF (see Figure 7). The outskirts of the Clouds show a tendency for the MDF to tend toward symmetry, which may be an indication of relatively metal-richer stars originating in the inner disk having migrated outward. This is particularly the case for the easternmost edge of the SMC indicated by the region of black pixels at an MS longitude of $\sim -8°$. Curiously, this region coincides (in projection) with the point at which the outer southern LMC spiral arm structure appears to join with the SMC (see Figure 1). On closer inspection, we see there is a population of giants with [Fe/H] $> -1$ dex in this region, relatively metal rich for outer SMC stars that generally take on [Fe/H] $< -1.3$ dex in our sample. It is plausible therefore that there exists a stripped LMC giant population in the region, which is the continuation of the outer spiral-like arm seen in Figure 1.

Considering both Clouds individually, we show the mean metallicity, stellar density, and associated extinction maps in Figure 9. Here, we show our giants in coordinates offset from the respective Clouds, adopting an LMC center of $(\alpha_0, \delta_0) = (82.^\circ25, -69.^\circ50)$ as determined by van der Marel & Cioni (2001) and an SMC center of $(12.^\circ60, -73.^\circ09)$ from Rubele et al. (2015). Again, the central bar is prominent and

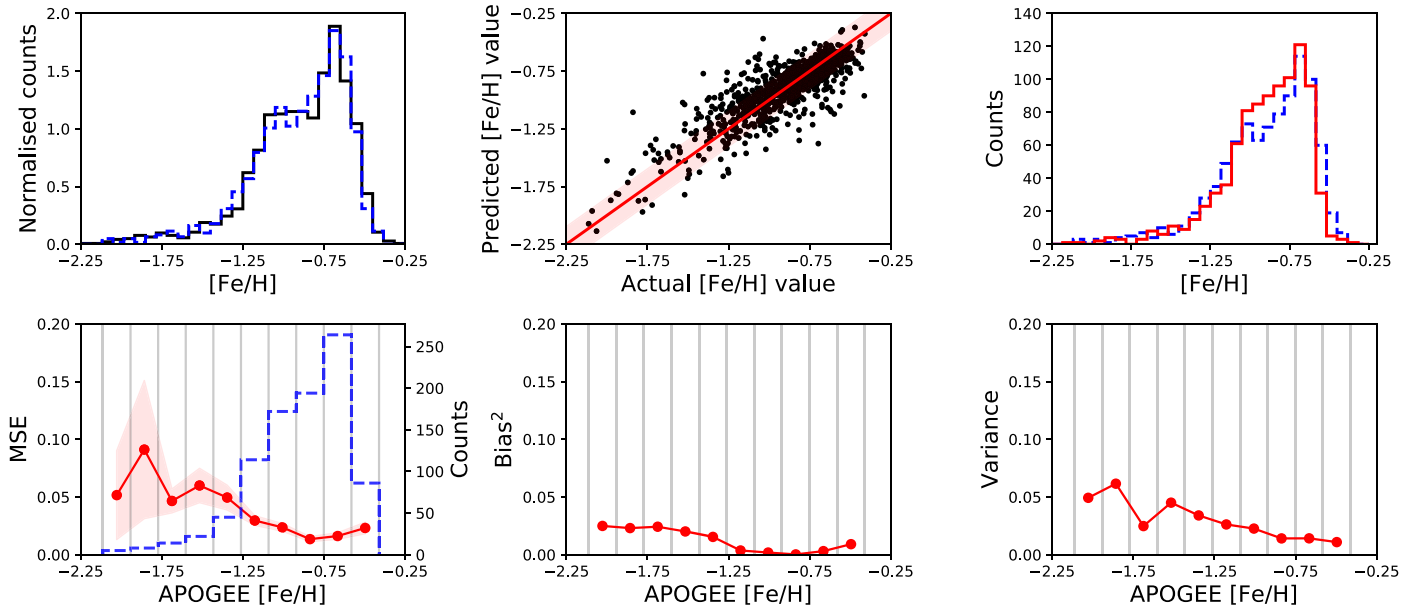


**Figure 6.** Upper-left panel: training data metallicity distribution in black solid line which is adequately representative of the test data distribution shown as the blue dashed line. Upper-middle panel: scatter plot of the predicted and APOGEE measured metallicities for the stars in our test set. The solid red line indicates a one-to-one correspondence, and the red shaded region bounds the RMSE of 0.15 dex recovered from the test set analysis. The majority of the scatter is present at the lowest of metallicities where the stellar density is extremely low. Upper-right panel: the blue dashed line indicates the test set's true metallicity distribution now overlaid with the predictions in solid red. Generally, the overall distribution is reproduced well. Lower left: the red line shows the estimated MSE binned by APOGEE metallicity values of our test data. The filled shaded region bounding this line shows the dispersion of this value weighted by the Poisson noise in each bin. The blue histogram shows the metallicity distribution of the test set in question, with the faint gray vertical lines indicating the bin edges. At metallicities less than $\sim -1.2$ dex, the corresponding RMSE is 0.23 dex. Lower middle: the squared bias in each metallicity bin is seen to be relatively low across the full range, with the greatest contribution being at the metal-poor end. Lower right: the variance of the predictions in each bin is shown. The largest contribution to total error is again seen at the metal-poor end owing to the dearth of training data in this region.

**Table 1**
Regression Errors

| [Fe/H] Bin | $\sigma_{[\mathrm{Fe/H}]}$ (dex) |
|---|---|
| $[\mathrm{Fe/H}] \leqslant -1.5$ | 0.25 |
| $-1.5 < [\mathrm{Fe/H}] \leqslant -1$ | 0.18 |
| $-1 < [\mathrm{Fe/H}] \leqslant -0.5$ | 0.13 |
| $[\mathrm{Fe/H}] > -0.5$ | 0.21 |

**Note.** The table lists the RMSE, computed from our test set predictions, in four metallicity bins. It is in the tails of the metallicity distribution that our predictions suffer greatest from total error, as demonstrated in Figure 6.

appears to display an extended metal-rich association just north of it; this extension is most likely the main spiral arm of the LMC. On slightly decreasing the dynamic range of the pixel color, a plethora of diffuse metallicity features within the LMC is revealed in the figure, notably the strikingly spiral-like feature in the southern portion of the disk, reaching down to $\sim 6^\circ$ below the LMC center. Its morphology is relatively smooth and coherent until $(\Delta L,\ \Delta B) \sim (2^\circ,\ -5^\circ)$, beyond which the metallicity structure becomes clumpy. This spiral-like feature, while faint, can also be seen in the corresponding stellar density map. The lack of correlation with any large-scale extinction patterns, seen in the rightmost panel, supports the notion of this being a genuine feature of the LMC disk. When comparing our LMC metallicity map with that of Choudhury et al. (2016), the large-scale features are generally consistent. In their analysis, they combined giants from the Optical Gravitational Lensing Experiment (OGLE-III) and Magellanic Cloud Photometric Survey (MCPS) out to a radius of $\sim 5^\circ$. Taking the slope of the RGB as a proxy for average metallicity, calibrated against spectroscopic data, they estimated the metallicity of subregions through the Cloud. Both samples provide reasonable coverage of the central LMC, with the OGLE-III (MCPS) footprint covering more of the east–west (north–south) regions. They observed the LMC bar to be the most metal-rich region and found evidence for a differing metallicity gradient through different regions of the disk; a shallower gradient was observed in the north–south regions in comparison to that in the east–west regions of the LMC. Both of these features are evident in Figure 9, where the metal-enhanced substructures in the top-left panel are seen to reside largely in the north–south direction where they act to flatten any preexisting gradient. With regard to the SMC, it is only the core of the dwarf that displays any coherent metallicity structure, consistent with the spatial density patterns observed by El Youssoufi et al. (2019) and the recent SMC metallicity maps of Choudhury et al. (2020). The outskirts of the SMC appear to be stretched and show an elliptical appearance, likely a result of tidal stripping of material through LMC interactions (see also Belokurov et al. 2017; Massana et al. 2020). The black dashed (dotted) lines in the figure denote selection bounds to sample giants lying along the projected major (minor) axis of the Magellanic bars for use in Section 4.1. Owing to the complex three-dimensional structure of the SMC, the exact orientation at which we are viewing it is highly uncertain, and so in this case, the bar selection is made simply to isolate the central-most metal-rich feature. It is worthwhile to note that, while the stellar density of our data set in the central regions of the Clouds is patchy and incomplete, we can still gain insight into the structure of these regions through the lens of spatially averaged metallicity maps. The spatial incompleteness in these regions is likely an effect of

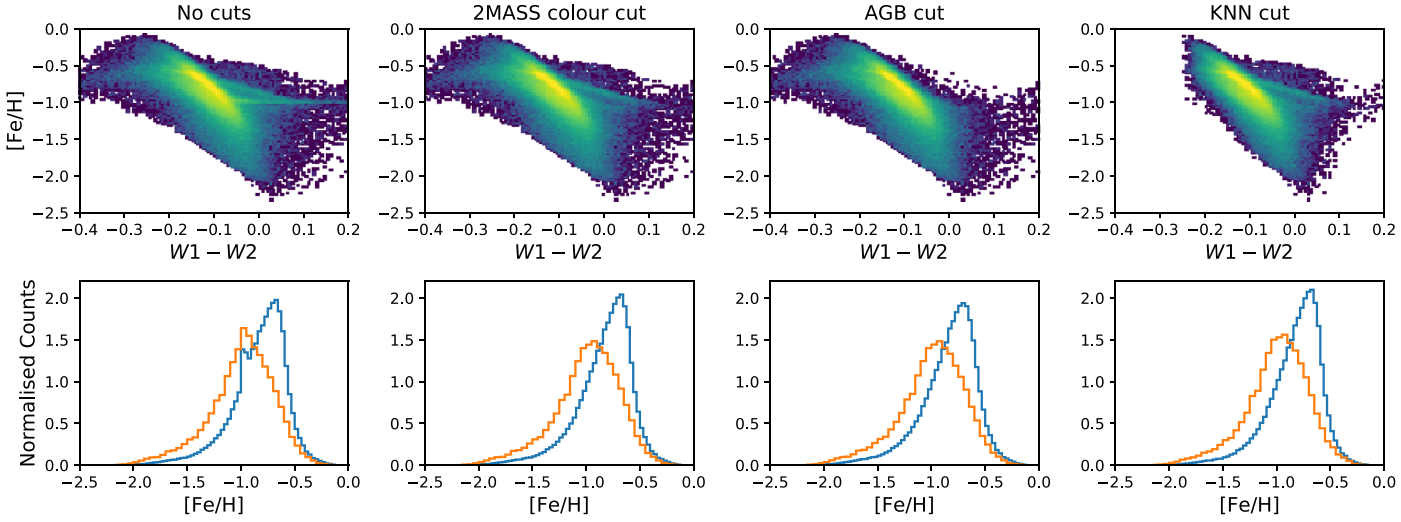


**Figure 7.** Predicted metallicities for our Gaia+2MASS+WISE giants as a function of WISE color W1 − W2 are shown in the top row. The bottom row shows histograms of the predictions for LMC (SMC) in blue (orange), selecting stars that fall within a 12° (8°) aperture of the respective Cloud. These histograms have been normalized to encompass an area of unity. In the leftmost panels, there is a population of stars for which our predictions are spurious, causing a pile-up at ∼−1 dex. These stars are the reddest stars in our sample and can be removed through the application of the 2MASS color cuts described in the text. The AGB stars form a bifurcation in the metallicity–color sequence owing to the unusual properties of the WISE isochrone tracks in which the AGB stars sharply turn red, crossing RGB tracks of lower metallicities. In turn, this causes a bimodality in metallicity at fixed WISE color. The final column shows the effect of requiring the mean feature space distance $\langle D_{NN} \rangle$ to be less than 0.06. It largely removes the stars that are extremely blue, culling those stars whose predictions spuriously converge to ∼−0.8 dex.

the CMD giant selection employed by Belokurov & Erkal (2019).

### 4.1. Metallicity Gradients

We first attempt to quantify the presence of a metallicity gradient within the LMC by considering the Cloud as an inclined thin disk. The equations of van der Marel & Cioni (2001) provide the transformations into a Cartesian system of an inclined thin plane, from observed on-sky positions, defined by its inclination angle $i$ and position angle $\theta$ measured counterclockwise from the west.[2] This allows us to assign each LMC giant an in-plane Galactocentric cylindrical radius $R$. We model the radial metallicity profile by the simple linear relationship:

$$[\mathrm{Fe/H}]^{\mathrm{model}} = \Theta_0 R(\alpha, \delta, i, \theta) + \Theta_1, \tag{2}$$

where we wish to infer the gradient and intercept contained in the parameter vector $\mathbf{\Theta} = [\Theta_0, \Theta_1]$. The in-plane radius is a function of the plane geometry and thus dependent on the choice of $(i, \theta)$ for the LMC. We account for this in our inference by marginalizing over these parameters. We fix the center of the LMC to be at $(\alpha_0, \delta_0) = (82.^\circ25, -69.^\circ50)$ as in van der Marel & Cioni (2001) and specify a distance of 49.9 kpc (de Grijs et al. 2014) to the LMC center. Writing the total likelihood as

$$p([\mathrm{Fe/H}]|\Theta, i, \theta, \alpha, \delta, \sigma_{\mathrm{Fe/H}}, V) = \prod_n^N \frac{1}{\sqrt{2\pi s_n^2}} \exp\left(-\frac{([\mathrm{Fe/H}]_n^{\mathrm{model}} - [\mathrm{Fe/H}]_n)^2}{2s_n^2}\right), \tag{3}$$

where $[\mathrm{Fe/H}]_n$ is our metallicity prediction for the $n$th giant. The term $s_n^2 = \sigma_n^2 + V$ encompasses the prediction error $\sigma_n$ for each giant and some general intrinsic scatter in the model through the parameter $V$. The full posterior probability can then be written as

$$p(\Theta, V|\alpha, \delta, [\mathrm{Fe/H}], \sigma_{\mathrm{Fe/H}}) \propto \int\int p([\mathrm{Fe/H}]|\Theta, i, \theta, \alpha, \delta, \sigma_{\mathrm{Fe/H}}, V) \times p(\Theta, V)p(i, \theta)di\, d\theta, \tag{4}$$

from which we can draw samples in a Markov Chain Monte Carlo fashion, utilizing the sampler `emcee` of Foreman-Mackey et al. (2013), for parameters $\Theta$ and $V$. In practice we compute the marginalization over the nuisance parameters $(i, \theta)$ by summing the likelihood over a two-dimensional Gaussian grid with mean $(i, \theta)$ values of 30° and 235°. The covariance matrix of the Gaussian prior was forced to be diagonal with respective widths of $\sigma_i = 5^\circ$ and $\sigma_\theta = 10^\circ$. These choices reflect the range of values reported in the literature; recently, Choi et al. (2018b) inferred an LMC inclination and position angle of $(25.^\circ86, 149.^\circ23)$ from photometric data alone whereas van der Marel & Kallivayalil (2014) infer viewing angles of $(34.^\circ0, 139.^\circ1)$ from field proper motions and old stellar line-of-sight velocities (note that in both these cases, the quoted position angle is in the usual astronomical convention). We perform the fit on all giants within a 12° aperture of the LMC. We also exclude the most central giants within $3.^\circ5$ so as to avoid the metal-rich bar and focus on stars primarily tracing the LMC disk. In doing so, we also mitigate the fact that our metallicity predictions for the most metal-rich stars, which dominate centrally, incur a degree of bias (∼0.1–0.2 dex) in our regression model. We further limit our analysis to giants with $\langle D_{NN} \rangle < 0.06$ to remove giants whose photometric colors lie in the domain in which our regression struggles to perform adequately. In doing so, we limit our sample to 196,216 RGs. We recover a metallicity gradient of $-0.048 \pm 0.001$ dex kpc$^{-1}$ for our giant sample, consistent with that of Choudhury et al. (2016), who found a gradient of $-0.049 \pm 0.002$ dex kpc$^{-1}$ in their analysis of LMC RGBs, as well

[2] Note that the usual astronomical convention is to measure position angle from north and is related to $\theta$ by PA $= \theta - 90^\circ$.

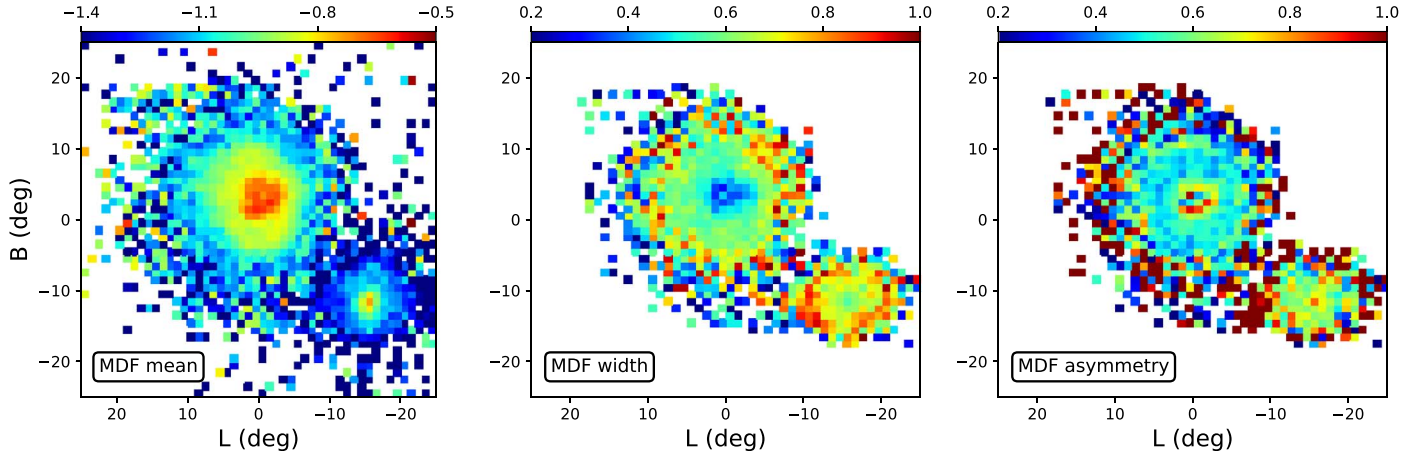


**Figure 8.** Left: average metallicity maps of the Clouds colored by mean metallicity per pixel. The central regions of the LMC are metal rich, with the region occupied by the LMC bar and dominant spiral arm. Outside the bar region, diffuse metal-rich structures are seen with an arc-like morphology in both the southern and northern regions. A negative metallicity gradient is seen through the LMC disk with apparent asymmetry; the northern and southern portions of the dwarf appear to have relatively more metal-rich stars at larger radii, and hence a flatter gradient, as opposed to the east–west direction. The outermost regions of the LMC are littered with metal-poor stars. Our metallicity predictions show the SMC to be distinctly more metal poor, with a slight gradient and central enhancement visible. Middle: we show the difference between the 90th and 10th percentile of [Fe/H] in each pixel, effectively a width measure of the MDF. The central regions of the LMC appear to have a relatively narrow MDF where the metal-rich bar and spiral arm dominate. Generally, the MDF of the SMC appears to be broader throughout the dwarf, in comparison to the LMC, likely owing to its large extent along the line of sight such that we are viewing a projection of multiple populations within the galaxy. Right: we color pixels by the ratio of the difference in the 95th and 50th to the difference in the 50th and 5th metallicity percentiles. A symmetric distribution would have a ratio of unity, with a left (right) skew having values below (above) this. It can be seen that regions near the LMC bar have values close to unity, a consequence of metal-rich stars being relatively more prevalent in this region acting to reduce the left skew of the MDF.

as that of Cioni (2009), whose value of $-0.047 \pm 0.003$ dex kpc$^{-1}$ was obtained from a sample of LMC AGB stars. For our intercept term, we recover a value of $-0.656 \pm 0.004$ dex. In Figure 10, we show the radial metallicity profile of our LMC giants. Our fit describes the negative profile well through the LMC disk, with the inner regions being the most metal enhanced. We show the metallicity profiles along the major and minor axes of the projected bar for both Clouds in Figure 11; the giants used in the figure were selected to lie between the dashed and dotted lines in Figure 9, respectively. For the LMC, we rotate into a coordinate system that is approximately bar aligned through a clockwise rotation of 30° into the system we denote ($L_{\rm rot}$, $B_{\rm rot}$). In the MS coordinate system, the major axis of the SMC bar is very nearly aligned with the vertical and so no rotation was performed. Both of the Clouds display a flattening of their metallicity profiles centrally in the bar-dominated regions. Outside of this domain, the profiles show clear negative gradients outwards into the disk. This is consistent with the findings of Fraser-McKelvie et al. (2019), who studied a sample of 128 barred galaxies, finding both the age and metallicity gradients to be flatter in the bar as opposed to the disks of the galaxies, indicative of bars being confined structures, efficient in radially mixing their stellar populations (see Seidel et al. 2016 also). Through the LMC disk, complex structure is observed with asymmetric gradients and plateau features present. The black solid line in these panels shows our model projected into this coordinate system to highlight the large degree of asymmetric metallicity structure that exists throughout the LMC; the western portion of the disk (i.e., toward positive $\Delta L_{\rm rot}$) shows a depletion in metallicity with respect to the model whereas the northern and southern regions show mild excesses. While we have hesitated to quantify the metallicity gradient in the SMC, owing to the uncertainty of the dwarf's morphology, Figure 11 demonstrates asymmetric gradients in the smaller Cloud also.

In Figure 12, we compare the mean metallicity maps of our LMC giants with that of an inclined disk whose radial metallicity profile follows that in our inference. The rightmost panel shows the metallicity residual, obtained by subtracting the model from the data, in which the LMC bar and main spiral arm are clearly revealed as centrally enhanced regions. The main spiral arm of the LMC is a feature usually only observed in young stellar tracers (ages $\lessapprox$1 Gyr) such as main-sequence stars and supergiants (e.g., Cepheid Variables), notably so in the recent morphological mapping of the LMC by El Youssoufi et al. (2019) using data from the VISTA survey of the Magellanic Clouds (VMC). Utilizing stellar synthesis models to calibrate stellar ages, they obtain age estimates for LMC stellar populations right across the CMD. Panels (B), (C), and (H) of their Figure 5 show the extent of the main spiral arm, with an additional faint arm emerging to the north of it; such a bifurcation is revealed in our metallicity residuals also and is annotated in the figure as a spiral extension. In the northern regions of the outer disk we isolate an arc-like area of metallicity enhancement. This portion of the LMC is coincident with the structure labeled "Arc" in Figure 3 of Besla et al. (2016), lying ∼5°–7° above the LMC center with no symmetric counterpart in the southern regions.

This feature is likely a remnant of tidal interactions between the Clouds. Indeed, the simulations of Besla et al. (2016) suggest that it is repeated close encounters between the Clouds that seed such stellar arcs in the northern periphery of the LMC, in isolation of the MW. This notion is supported by the observation of the Clouds appearing to be on their first infall (see, e.g., Besla et al. 2007; Kallivayalil et al. 2013). The curious spiral-/arc-like feature seen in Figure 9 is also revealed in Figure 12, which we label as the Southern Arm, wrapping from ∼−4° to 2° in latitude and looks to emanate from the bar downwards by ∼6°. This feature is curious in its apparent asymmetry, with typical spiral galaxies possessing spiral arms

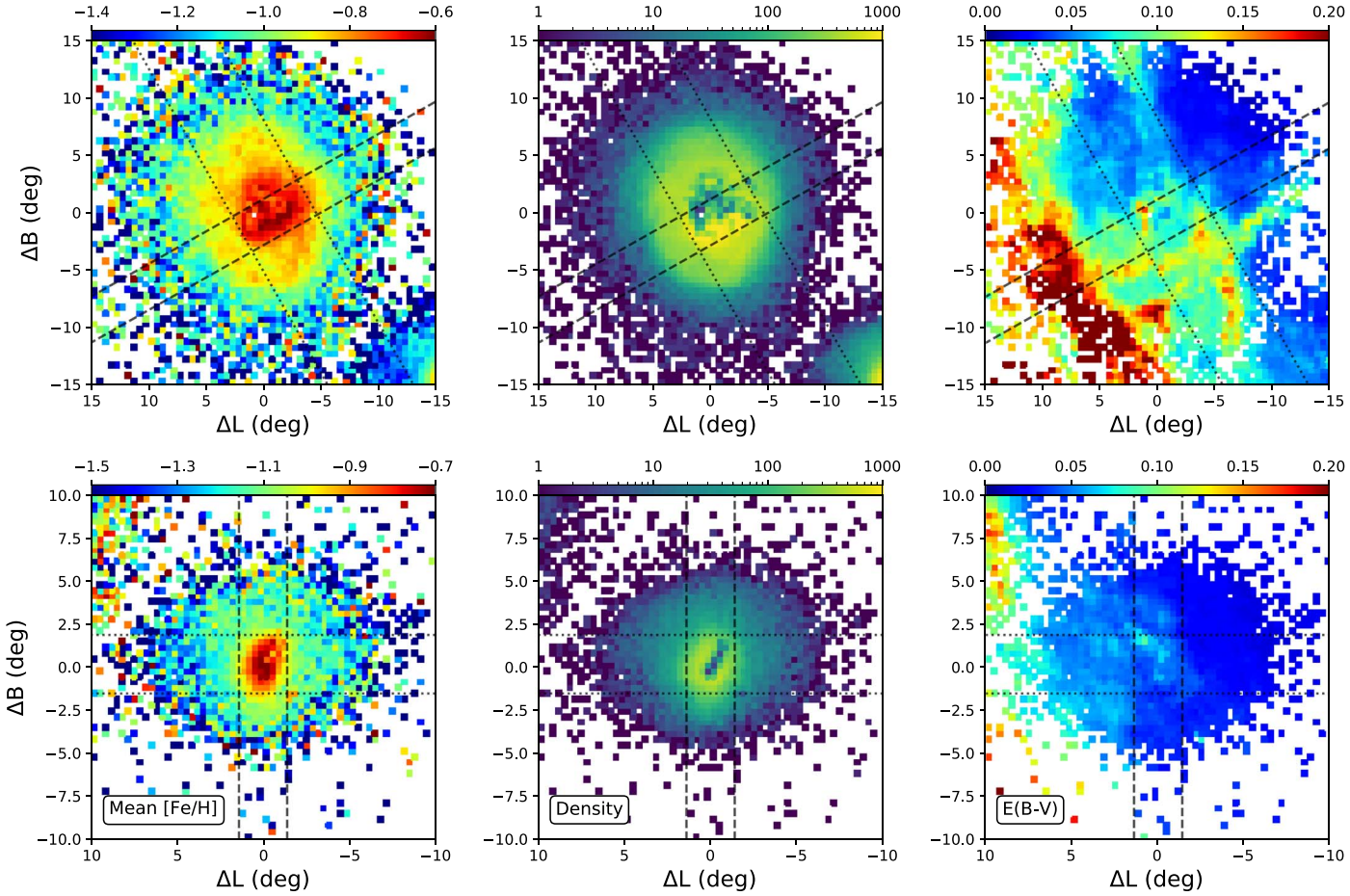


**Figure 9.** Top (bottom) row of the figure corresponds to the LMC (SMC). The left column shows the mean metallicity per pixel. The same general features are seen as in Figure 8, with the central regions of both Clouds being the most metal-rich and diffuse metal-enhanced structures seen in the outer LMC disk. The middle column shows the stellar density map of the Clouds; central regions of high extinction are most affected, yielding gaps in the density profile. The SMC displays a stretched morphology with wings on the eastern and western sides of the dwarf, a consequence of the tidal interactions with the LMC. The right columns show the extinction map adopted in this work. Generally, the extinction is low aside from the eastern side of the LMC lying nearest the Galactic plane and various filamentary structures throughout it. Stars that fall between the dashed (dotted) lines are those shown in Figure 11 to trace the metallicity profile of the LMC and SMC along the projected major and minor axes of their respective bars.

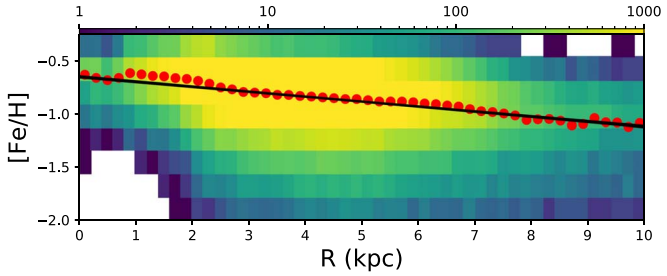


**Figure 10.** This shows the evolution of LMC giant predicted metallicity as a function of in-plane cylindrical radius. Pixels are colored by stellar counts per pixel. The central regions are seen to be metal enhanced with respect to the outer regions of the LMC, where the metal-rich bar dominates. The red markers show the mean metallicity in bins of radius. A shallow negative metallicity gradient is evident. The solid black lines are samples drawn from our model. We only show giants with $\langle D_{NN} \rangle < 0.06$ in this figure to isolate stars that should have reasonable metallicity estimates given their colors. In this figure, we adopt the LMC viewing angles of Choi et al. (2018b).

emanating symmetrically from the bar. This residual feature is largely coincident with the ring-like overdensity uncovered by Choi et al. (2018a). Through modeling the LMC stellar density with a disk and bar component, their residuals revealed a structure akin to ours composed of stars older than ∼1 Gyr. They observe the feature to wrap around more extensively on the western side of the LMC in comparison to our metal-rich feature, which diminishes at $(\Delta L,\ \Delta B) \sim (2^\circ,\ -6^\circ)$ in our residuals and is more reminiscent of a spiral/arc as opposed to a ring. Curiously, however, the signal of their overdensity appears to diminish in strength near the tip of our residual spiral. Beyond this, the Choi et al. (2018a) overdensity becomes patchy as it continues to wrap around the LMC center. Looking at our data in the left panel of Figure 12, we observe similar behavior; the coherent spiral-like structure emerges from the southwest end of the bar and wraps eastward until $(\Delta L,\ \Delta B) \sim (2^\circ,\ -6^\circ)$, beyond which we see a patchy continuation of slight [Fe/H] enhancement. El Youssoufi et al. (2019) also saw evidence of such a southern structure in their analysis of VMC data, with aging main-sequence stars and subgiants (∼1–2.5 Gyr) a faint extension from the southwest region of the bar. Bica et al. (2008) mapped the spatial distribution of Magellanic star clusters (ages <4 Gyr), indeed observing a southern spiral/ring-like structure that our metal-rich feature is spatially coincident with.

We attempt to determine if our Southern Arm giants are kinematically distinct in any way by considering their proper motion dispersions. To do so, we first select all pixels bound by

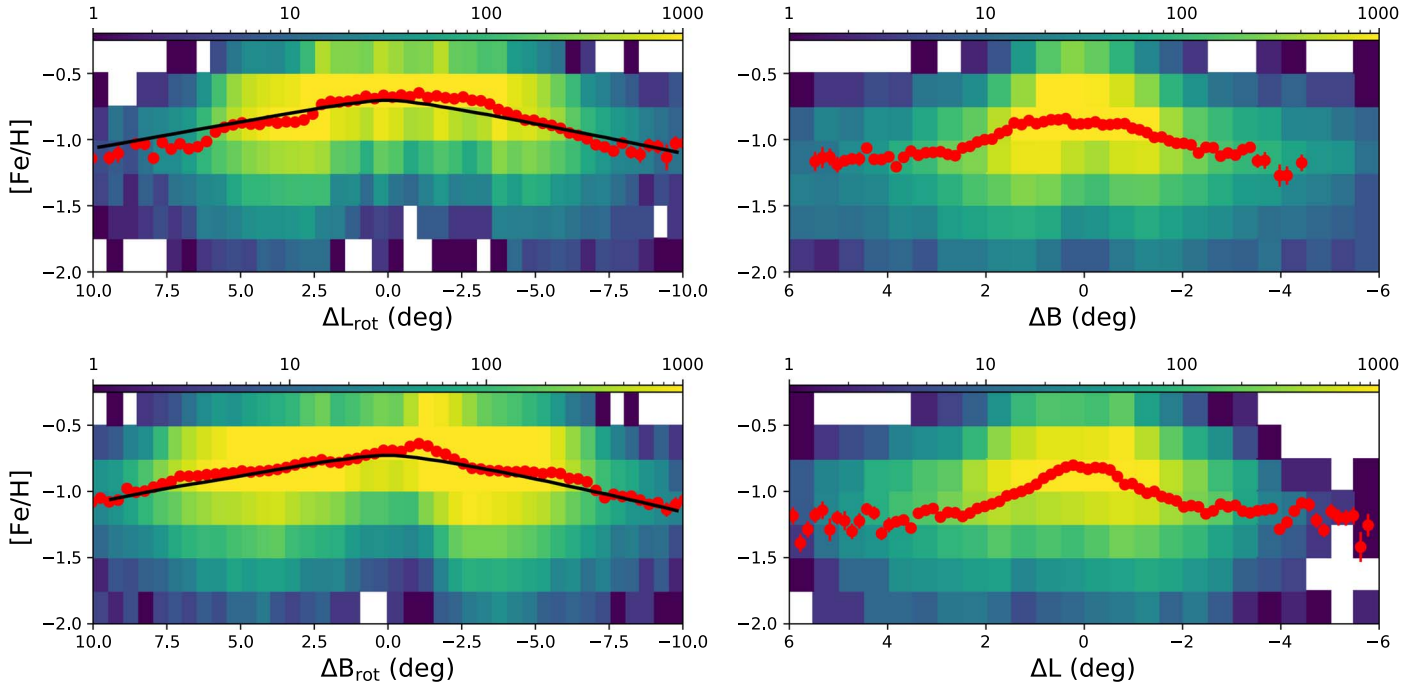


**Figure 11.** Stellar density maps tracing the metallicity profile along directions aligned with the projected axes of the bars. The left two panels correspond to the LMC and the right panels to the SMC. The top (bottom) row shows the profile of stars that fall within the dashed (dotted) line in Figure 9. In the case of the LMC, we have rotated the Magellanic Stream coordinate system clockwise by 30° so as to approximately align with the major axis of the bar. We only consider stars with $\langle D_{NN} \rangle < 0.06$ in this figure. Red markers correspond to mean metallicity binned over angular offset relative to each Cloud's center, with error bars representing standard errors in each bin. Both the LMC and SMC show a flattening in the metallicity profile centrally in the domain of the bar. Clear negative gradients are observed on increasing distance away from the central regions, with strong asymmetries and plateau-like features present.

the polygon in Figure 12. We further select all pixels within a 5°–7°.5 aperture around the LMC center, rejecting those within the polygon, to represent stars at a similar radius to the arm for a "local" comparison. We also select metal-rich pixels associated with the LMC bar. As a simple investigation, we plot the histograms of pixel proper motion dispersion in Figure 13 where we see both disk populations coexist in proper motion dispersion, distinctly cooler than the bar region. This combined with the fact that this spiral-like structure is a metal-rich feature is suggestive of it harboring LMC disk stars. We conjecture that these stars may have been perturbed in some way, giving rise to the coherent, spiral-like structure we see. Many barred galaxies display a symmetrical appearance, with spiral arms emerging from both ends of the bar. The LMC however has long been known to possess only one dominant spiral arm. Recently, Ruiz-Lara et al. (2020) determine the LMC spiral arm to be a spatially coherent structure that has been in place for the last ∼2 Gyr, supporting the notion that it was seeded through a historic close encounter with the SMC, as observed in simulations (see, e.g., Besla et al. 2012; Pearson et al. 2018). The *N*-body simulations of Berentzen et al. (2003) demonstrate that the collision of a small companion with a larger barred galaxy can seed complex structures such as spiral arms, stellar rings, and stellar spurs, and those of Walker et al. (1996) further display the prominence of one-sided spiral features seeded by the accretion of a satellite galaxy onto a large disk galaxy; single spiral arms emanate from the bar and wrapped spiral arms form in the disk. It is likely that the southern spur we observe has arisen from the historic interactions between the LMC and SMC and is a metal-rich counterpart of the structure observed by Choi et al. (2018b). Our residual maps show the northern and southern portions of the LMC to be metal enhanced with respect to the eastern and western regions, an observation consistent with that of Choudhury et al. (2016), indicative of the former regions being most disrupted by previous tidal interactions. The region of slight metallicity depletion, running interior to the Southern Arm, is evident in the top-left panel of Figure 11 as the plateauing region at $\Delta L_{\rm rot} \sim 3°$–5°, beyond which the metallicity diminishes as outer metal-poor stars begin to dominate. The two slight bumps in metallicity in the bottom-left panel of Figure 11 correspond to the northern arc and Southern Arm features we present in Figure 12. Thus, while our giant sample is incomplete and much of the LMC structure difficult to discern from our density maps alone, we utilize our metallicity estimates as a probe into the LMC disk structure. In considering the deviation away from a smooth, simple axisymmetric metallicity model, we readily observe the complex structures that are known to reside in the LMC disk at once, in effect overcoming the completeness limitations of our sample.

### 4.2. Slicing the Clouds by Metallicity

We consider the broad-scale morphology of the Clouds as a function of metallicity in Figure 14 where we show the stellar density in the three metallicity bins of [Fe/H] $< -1.1$, $-0.9 <$ [Fe/H] $< -0.75$, and [Fe/H] $> -0.65$, each containing ∼44,000 giants. We will refer to these bins as M1, M2, and M3 hereafter. Although there exists a degree of scatter between the bins due to the uncertainty in our metallicity predictions, we present this map to provide a sense of the general structural trends of the Clouds on increasing metallicity. The majority of the outer substructure around the Clouds is made of the metal-poorer stars in M1. It is in this bin that the northern substructure identified by

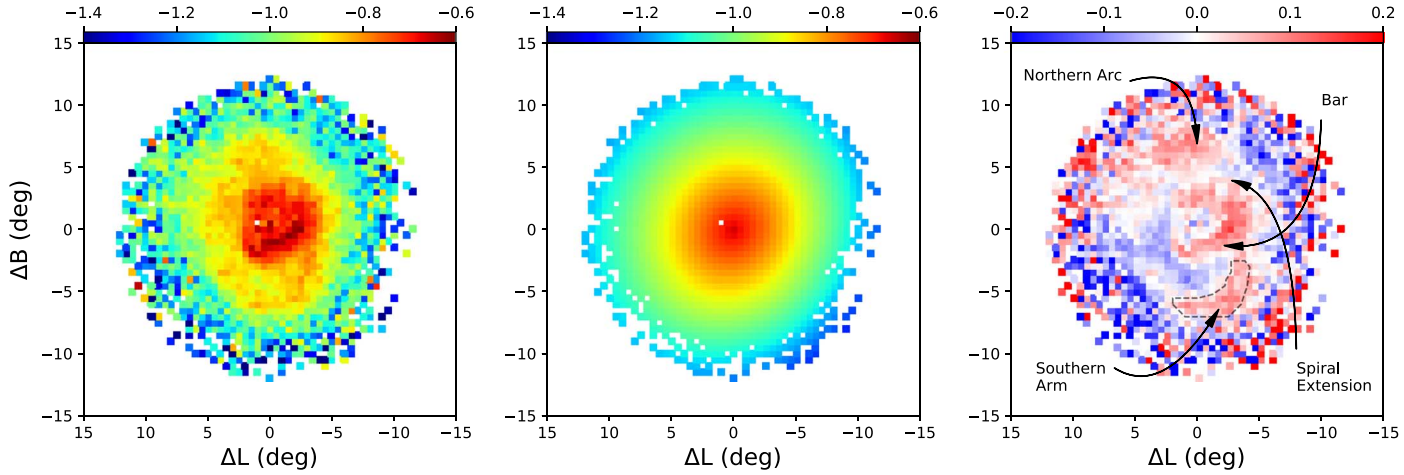


**Figure 12.** Left panel: giants within 12° of the LMC are shown in Magellanic Stream coordinates (relative to the LMC center) with pixels colored by mean metallicity. The metal-rich central region traces the bar and the dominant spiral arm of the Cloud. The northern portions of the disk trace arc-like features and the southern region shows a spiral-like feature with moderately enhanced metallicity. Middle panel: mean metallicity map of and inclined disk with viewing angles of Choi et al. (2018b) and radial metallicity function defined by the parameters found by out fitting method. Right panel: we subtract the metallicity of the model pixels from that of our data to highlight regions that are enhanced/depleted with respect to a disk whose radial metallicity distribution follows the form of Equation (2). Red pixels correspond to metal-richer regions and blue pixels to metal-poorer ones with respect to the model. The most striking revelation in doing this is that of the LMC's metal-rich bar and inner northern spiral arm emanating from the northwest end of the bar. Giants used to make this figure were subject to our nearest neighbor selection in feature space. Prominent regions, other than the bar, of enhanced metallicity are annotated and labeled.

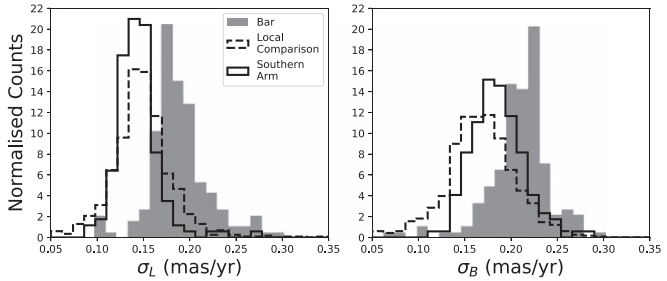


**Figure 13.** Histograms show reflex-corrected proper motion dispersions in the Magellanic Stream coordinate system ($L$, $B$). We have normalized the histograms such that their areas integrate to unity. The black-lined histogram corresponds to pixels bound by the polygon in Figure 12 and the dashed-line histogram is stars bound by the aperture described in the text. The gray histogram represents the metal-rich pixels in the LMC bar region ,which are distinctly hotter than the two disk populations. Stars in the Southern Arm appear to share similar dispersions to those lying at a similar (projected) radius across all azimuthal angles.

Mackey et al. (2016) is most prominent. A region at the base of this structure was recently analyzed by Cullinane et al. (2020), finding it to be kinematically perturbed from an equilibrium disk, likely through SMC/MW interactions. Furthermore, the southern stellar stream-like feature that connects to the SMC, first observed by Belokurov & Erkal (2019), is only apparent in this bin and appears to be the symmetric counterpart to the northern outer arc. The LMC+SMC+MW $N$-body simulations conducted by Belokurov & Erkal (2019) found that as recently as ∼150 Myr after a close encounter with the SMC, such outer spiral-like features can be induced in the LMC. Indeed, the SMC is thought to have experienced a direct collision with the LMC on a timescale comparable to this from the kinematical modeling of Zivick et al. (2018). Another diminishing feature with increasing metallicity is the density of stars in the old stellar MB region, likely composed of outer, tidally stripped stars originating from both the LMC and SMC. The general shape of both Clouds also appears to evolve in a sensible way, presenting themselves as extended, rather than diffuse, objects at the metal-poorer end in M1 through to much more centrally concentrated objects at the metal-rich end in M3. In the case of the SMC, it demonstrates a degree of ellipticity in M1 (and slightly so in M2), indicative of the strong tidal disruption induced in the outer metal-poor regions.

We consider the proper motions of our giants in the three bins in Figures 15 and 16. We correct for the solar reflex motion assuming a constant heliocentric distance of 49.9 kpc (with the main focus being the LMC). The dominant signal is that of rotation within the LMC disk, apparent by the gradient across the Cloud. As in Belokurov & Erkal (2019), the northern and southern arm-like features display a coherent rotation signal, lagging that of the LMC disk; both arms bear motions that are consistent with the bulk of the LMC and appear distinct from the proper motions of the SMC. In Figure 15, a significant portion of the SMC nearest to the LMC shows prominent motion toward the larger Cloud, with the signal appearing to persist across the three metallicity bins. The lower-left panel of Figure 15 shows there to be significant dispersion in M1, precisely at the SMC edge of enhanced proper motion and at the LMC–SMC interface, where a mixture of Cloud populations is to be expected. The SMC is known to be disrupting (see, e.g., Zivick et al. 2018; De Leo et al. 2020) and the perturbed motions we observe here are likely a result of this, with the LMC violently dragging the eastern edge of the SMC toward it. The fact that we observe this signature in all three of the top panels indicates that the disruption is severe, penetrating through to the more centrally concentrated metal-rich giants in M3. With respect to the motions of $\mu_B$, the two main regions of significant heating appear in M1: at the base of the northern arm and another diametrically opposed to this in the southern region. Between these two points, we also observe a vertical region of moderate dispersion in the LMC. That is, the dispersion in $\mu_B$ is greater along the north–south direction than so along east–west. This may be a consequence of how the LMC has been perturbed by the SMC, as the majority of substructure observed in Section 4.1 is observed to lie in the northern and southern regions of the LMC disk. In each bin, the central bar region also displays a degree of enhanced

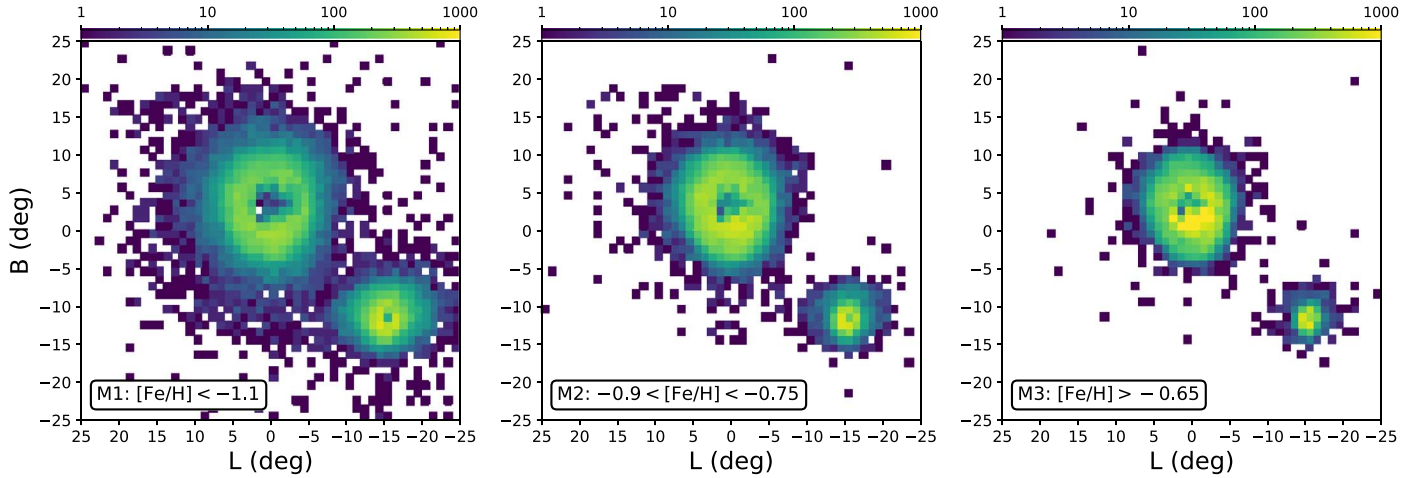


**Figure 14.** Stellar density maps of our red giants in the three metallicity bins described in the text with metal poor in the leftmost panel and metal rich in the right. The general evolution in morphology is a decrease in the outer substructure in both Clouds with increasing stellar metallicity. The most metal-rich bin shows the LMC and SMC to be isolated, whereas the metal-poor bin shows the Clouds to be connected, both in the Magellanic Bridge region and further south where the outer stellar arc of the LMC attaches to the eastern edge of the SMC. The most metal-poor giants in the SMC show a high central density, with the outer regions appearing stretched horizontally, likely due to tidal interactions with the LMC. At the metal-rich end, the SMC is much more compact and shows a weaker signature of tidal disruption.

dispersion, both in $\mu_{\rm L}$ and $\mu_{\rm B}$, owing to the complex orbits hosted by galactic bars.

### 4.3. SMC Shape and Disruption

In Figure 17, we show the density of stars lying around the SMC in MB coordinates. The top-left panel of the figure shows an ellipse fitted to an outer SMC density contour for which a mild ellipticity value of ∼0.21 is obtained. Upon plotting a set of isodensity contours to the SMC giants in the top-right panel, a distinctive twisting is seen, with the outer regions displaying an S shape that is characteristic of a tidally perturbed system. Similar SMC morphology was observed by Belokurov et al. (2017) in the Gaia DR1 data. They found that the orientation of the S-shaped tails aligned conspicuously with the SMC's proper motions vector (relative to the LMC). Based on this, they designated the tail nearest to the LMC to be the trailing arm and that stretching toward the top right in Figure 17 to be leading. In the lower panels of the figure, we have sliced the stars into two metallicity bins, symmetrically offset from the mean of our SMC metallicity distribution, so as to investigate the morphology of a relatively metal-poorer and metal-richer subset of SMC giants. The bottom-left panel of Figure 17 shows the stellar density of stars with $[{\rm Fe/H}] < -1.25$ dex. These metal-poorer giants constitute a relatively diffuse, fluffy population, with their outermost contour again showing the tidally symptomatic S shape. The bottom-right panel of the figure shows stars with predicted metallicities $[{\rm Fe/H}] > -0.75$ dex, and we show the same isodensity contours as in the metal-poor bin in black for comparison. The bulk of these metal-richer giants are confined to the most central regions, with little extent beyond ∼5° of the Cloud center. The red solid line traces the outermost contour level of the metal-poorer bin which highlights that the outskirts of these relatively metal-richer giants also show symptoms of tidal disruption.

We consider the motion of the SMC in a simple fashion by first studying the spatially averaged proper motion components in Figure 18. In the figure, we have set the origin of the coordinate system to the SMC center. The pixels in the left (right) panel are colored by mean $\mu_{X_{\rm MB}}$ ($\mu_{Y_{\rm MB}}$), where we have centered the proper motion distributions around the bulk values for our SMC giants. We compute these based on the mean proper motions of giants lying within a 3° aperture of the SMC for which we obtain the SMC motion to be $(\mu_\alpha, \mu_\delta) = (0.65, -1.21)$ mas yr$^{-1}$, consistent with the recent determination of De Leo et al. (2020) and similar to that of Zivick et al. (2018). We note that the RA component of our measured proper motion is smaller than that of recent ground-based measurements, with Niederhofer et al. (2018) measuring $(1.087 \pm 0.192, -1.187 \pm 0.008)$ mas yr$^{-1}$ from VMC data. We have also corrected the proper motions for the perspective expansion/contraction induced by the systematic center-of-mass motion along the line of sight, following van de Ven et al. (2006). The left panel of the figure shows stars residing on the edge nearest the LMC (on the side of the trailing tail), being pulled directly toward the larger Cloud, with giants on the opposite leading edge of the dwarf showing little sign of such effects. Further, the motion of the giants in $\mu_{Y_{\rm MB}}$ shows very little structure, with no indication of ordered rotation. Note that the faint vertical, banding structure seen in this panel is an artifact of the Gaia scanning law (see Gaia Collaboration et al. 2018c). Thus, in the picture we present here, it would seem that the region of the SMC nearest the LMC, and coincident with the trailing arm, is being violently hauled toward the LMC. Recent detailed kinematic analysis of SMC RGB stars by De Leo et al. (2020) found the dwarf to be undergoing strong tidal disruption, with a net outward motion of RGB stars in the direction of the LMC. The giants display strong tangential anisotropy in their proper motion dispersions, right down to the SMC center. Through comparison to a suite of *N*-body simulations of the Clouds in orbit about the MW, they argued that this effect is due to unbound material lying in front of the SMC, distinct in their kinematics due to tidal stripping by the LMC. The proper motion analysis of Zivick et al. (2018) also showed the SMC to bear little sign of ordered rotation, but rather mean ordered motion radially away from the galaxy in its outer regions, consistent with heavy disruption. The geometry of the SMC is complex, with a substantial line-of-sight depth. The northeastern regions of the dwarf appear to lie closer to us than its western edge, as perceived through numerous stellar tracers, including star clusters, red clump stars, Cepheid Variables, and RRL (see, e.g., Crowl et al. 2001; Haschke et al. 2012; Subramanian & Subramaniam 2012; Deb et al. 2015, 2019; Scowcroft et al. 2016; Muraveva et al. 2018). The SMC red clump

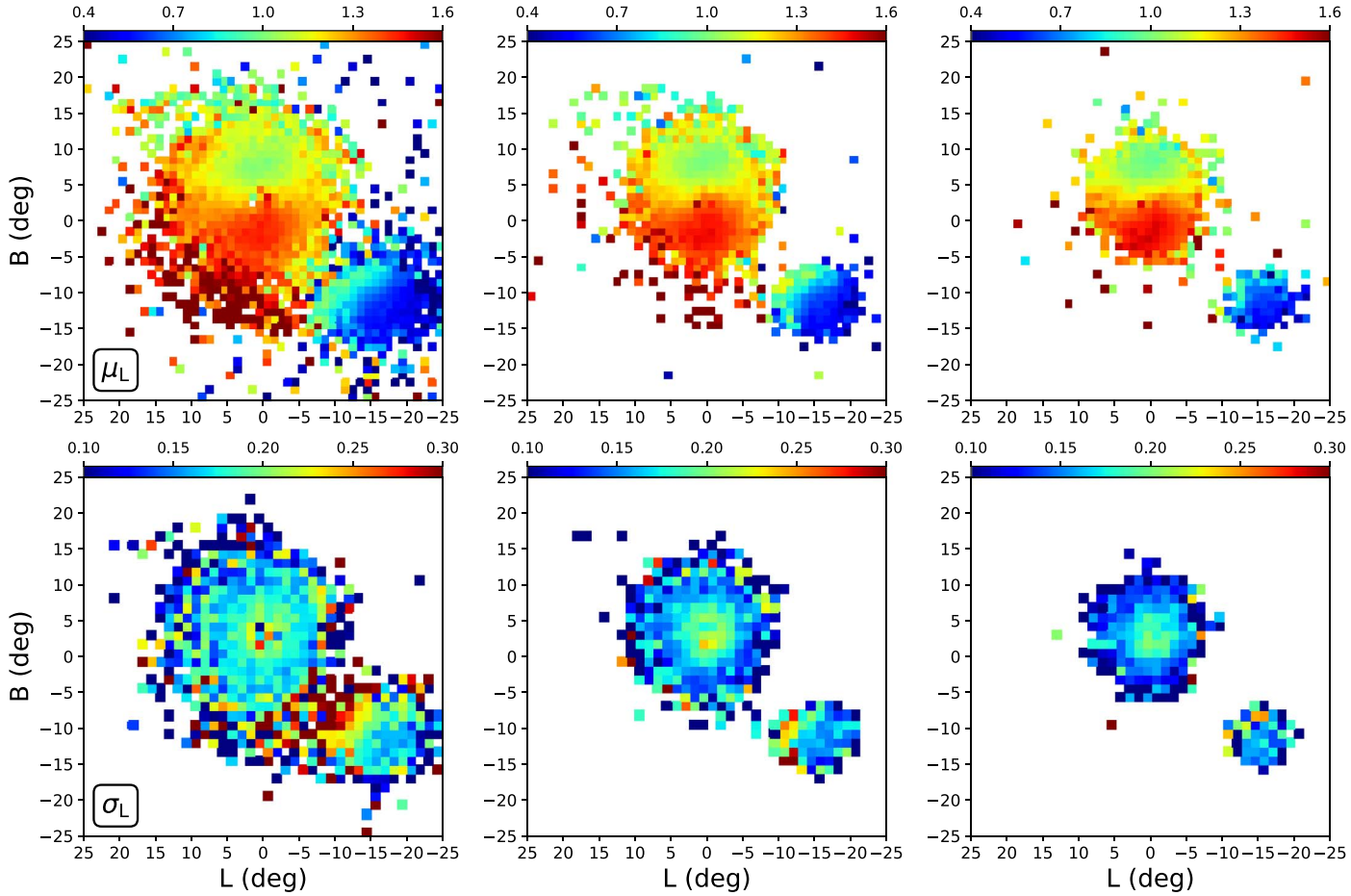


**Figure 15.** In the top panels, we show the reflex-corrected, mean $\mu_L$ in three metallicity bins M1, M2, and M3 as in Figure 14. The lower panels show the respective dispersion in each pixel. The LMC displays a coherent rotation signal across all the metallicity bins, with the two outer arms appearing to lag somewhat behind the inner disk. The SMC shows a gradient in its motion, with the edge nearest the LMC displaying prominent motion toward the larger Cloud. The greatest dispersion in the motion of the giants appears in the metal-poorest bin at the interface between the Clouds—a region where we expect mixing of stellar populations and turbulent motion due to tidal interactions within the system. The central-most region of the LMC, in the vicinity of the bar and spiral arm, is mildly visible as a region of enhanced dispersion.

analysis of Nidever et al. (2013) revealed a stellar structure lying eastward at ∼10 kpc in front of the dwarf, a structure they interpret to have been tidally stripped and dragged toward the LMC/MB region. Further to this, Subramanian et al. (2017) also found evidence for such a tidally stripped stellar structure in identifying a population of VMC red clump stars lying ∼12 kpc in front of the main SMC body, tracing them from the direction of the MB right down to ∼2°.5–4° of the SMC center. Very recently, Omkumar et al. (2021) identified this foreground red clump population in Gaia, tracing it from the inner 2°.5 out to ∼5°–6° from the center of the SMC. We attempt to discern whether those giants whose on-sky motion is prominently toward the LMC in Figure 18 are indeed lying closer to us as a result of tidal stripping by the larger Cloud. To do som we first select all SMC giants lying within the black dashed circle in Figure 18. We then attempt to use each star's relative position within the observed CMD as a proxy for heliocentric distance. We first select stars for which we have predicted metallicities in the range of $-1.2 < [\mathrm{Fe/H}] < -0.5$ dex, a region where there is sufficiently low bias and variance in our predictions that our estimates are reasonable. We then divide these giants into metallicity bins of width 0.2 dex and, considering each metallicity bin independently, fit a polynomial to the CMD of the giants, an example of which is shown by the solid red line in the upper-left panel of Figure 19, where we choose to utilize the CMD of $RP - H$ versus $H$ owing to the limited spread it displays at fixed metallicity and clear correlation. We do this to minimize the broadening of the CMD due to the spread in metallicities of the SMC population. Utilizing these polynomials fits as base "spines," we compute the magnitude offset $H - H_{\mathrm{spine}}$ for the selected SMC stars relative to the spine, such that stars with a negative (positive) offset are likely closer (farther) in distance. We only use stars that fall in the range $1.6 < RP - H < 1.9$, a region where the polynomial fits appear most reasonable and indicated in Figure 19 by the vertical black dashed lines. The upper-middle panel of Figure 19 shows the distribution of this magnitude offset, where we see it to be centered at zero and approximately symmetric. The histogram shows a slight skew toward negative values, indicative of a higher relative proportion of SMC giants lying in front of the dwarf's core. We then choose three bins in $H - H_{\mathrm{spine}}$ initially centered at −0.3 mag, 0 mag, and 0.3 mag, corresponding to ∼±10 kpc in front of and behind the SMC, with the bin edges shown by the red, green, and blue lines, respectively. We have then allowed the widths of the two outer bins to be broad so as to roughly equalize the counts per bin (3000) and to encompass stars lying in the tails of the distribution. The upper-right panel of the figure shows the logarithmic density of our selected SMC stars' spatial coordinate $X_{\mathrm{MB}}$ as a function of their motion in $\mu_{X_{\mathrm{MB}}}$ (approximately) toward

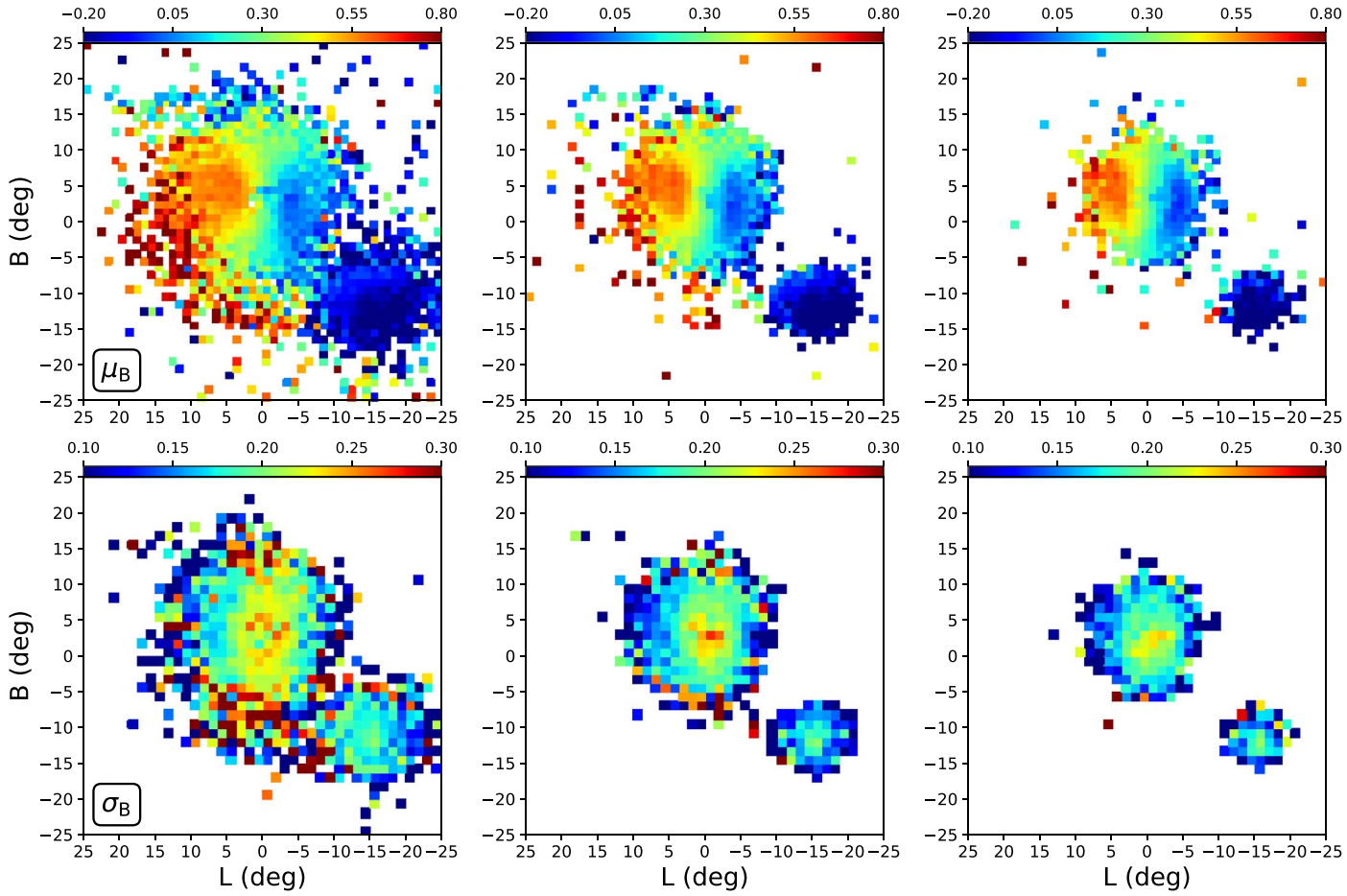


**Figure 16.** As in Figure 15 but pixels now colored by mean $\mu_B$ in the top panels and corresponding dispersions in the lower panels. Again, the dominant signal within the LMC is that of ordered rotation within the disk. The regions of most turbulent motion appear to exists at the bases of the two outer spiral-like features. Through the inner regions of the disk, there also appears to be enhanced dispersion in this direction in comparison to that of $\mu_L$. This is perhaps indicative of the tidal disruption endured by the LMC occurring mostly in the north–south regions where the majority of the stellar substructure is observed (see Figure 12).

the LMC. From this density plot alone, there is a clear population of stars with high $\mu_{X_{MB}}$ values, deviating from the bulk beyond $\mu_{X_{MB}} \sim 2°$. For the three distance bins we have defined, we show the mean proper motion binned over coordinate $X_{MB}$, where a clear distinction is observed between the different distance bins. At a value of $X_{MB} \sim 2°$, the stars most likely lying in front of the SMC display a sharp turn toward stronger motion in the LMC direction, dominating the population of stars exhibiting high values of $\mu_{X_{MB}}$. It therefore seems that the stars apparently being ripped from the SMC are predominantly those lying closer to us, tracing the disruption of the trailing arm down to the inner regions of the SMC. On increasing heliocentric distance, the signal diminishes with little sign of a companion leading arm in the proper motions. The bottom panels of the figure are colored by mean $\mu_{X_{MB}}$, where we show each of the three distance bins independently, with stars lying in front (behind) of the SMC in the left (right) panel and stars approximately at the SMC distance in the middle panel. The evolution of disruption with increasing distance is evident, with the closer stars being those most strongly dragged toward the LMC. Thus, our interpretation is that the portion of the SMC in which we see strong motion toward the LMC in Figures 15 and 18 consists largely of tidally stripped stars —stars that have been dragged outwards to closer heliocentric distances with their motions disrupted toward the larger Cloud, in effect forming a tidal tail trailing the SMC. We observe the signature down to angular separations of ∼2°–3° from the SMC center, indicative of heavy disruption of SMC stars lying along our line of sight. The fact that we do not observe a significant kinematic counterpart to the trailing tail lying beyond the SMC ( i.e., the leading arm) is somewhat at odds with simulation models of the Magellanic system. While the majority of simulations in the literature aim to primarily trace the gaseous features of the Clouds, those of Diaz & Bekki (2012) do well in replicating the general properties of the MB region, with signs of stars being drawn eastward and toward the LMC (see Nidever et al. 2013 for discussion). However, these models also predict a "counter-bridge," lying at large heliocentric distances and predominantly directly behind the SMC (see also Belokurov et al. 2017). Such a feature is predicted to be much more diffuse than its bridge counterpart, which may indicate why no stellar detection has been made, either in this work or by Nidever et al. (2013) and Subramanian et al. (2017). Indeed, the counter-bridge, if present, may be so diffuse that it exists as a purely gaseous feature with minimal stellar counterpart (see Diaz & Bekki 2012). Interestingly, however, in their analysis of SMC Cepheids, Ripepi et al. (2017) found evidence for a population of variables located toward the anticipated region of the counter-bridge.

We note that the stellar content of the SMC is complex, with stars spanning a range of metallicities and ages. In our above

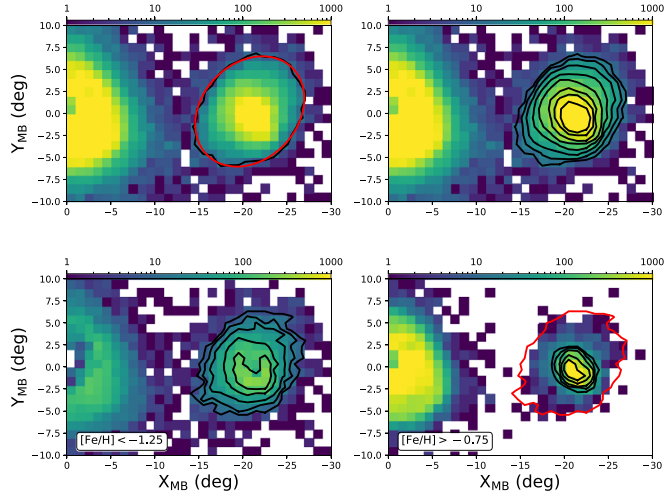


**Figure 17.** We show the stellar density of stars near the SMC in Magellanic Bridge coordinates. Top left: black solid line is an outer isodensity contour corresponding to 10 stars per square degree. We fit an ellipse to this contour, shown by the solid red line, whose ellipticity is mild at ∼0.21. Top right: we overlay logarithmically spaced isodensity contours on the SMC where a clear S shape is apparent, reminiscent of tidal tails and consistent with the RR Lyrae SMC morphology observed by Belokurov et al. (2017). Bottom left: we now only show giants with predicted metallicities of [Fe/H] $< -1.25$ dex and contours trace pixels corresponding to the 2.5th, 5th, 10th, 25th, and 50th percent contour level for stars around the SMC. Bottom right: we only consider stars with [Fe/H] $> -0.75$ dex and trace the same contour levels with black solid lines. The red line corresponds to the outermost contour of the metal-poor SMC giants. While the metal-rich giants are located much more centrally within the SMC, the outer regions still bear the signature of tidal disruption, indicating that the SMC has been significantly disrupted across a range of stellar populations.

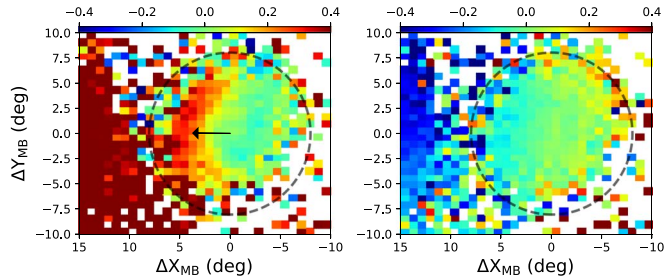


**Figure 18.** SMC giants shown in the Magellanic Bridge coordinate system. Pixels in the left (right) panel are colored by mean proper motion along $X_{\rm MB}$ ($Y_{\rm MB}$). The black arrow in the left panel points toward the center of the LMC in this system. There is little sign of internal motion in $\mu_{Y_{\rm MB}}$ with a distinct lack of rotation signal. In the left panel, a clear gradient is seen with SMC giants residing on the side nearest the LMC clearly being disrupted toward the larger Cloud.

analysis, we have alleviated the effect that metallicity has in broadening the CMD. We cannot, however, account for the fact that giants of differing ages, at fixed metallicity and distance, will induce a magnitude offset in $H - H_{\rm spine}$. Thus, our distance proxy is rather a convolution of heliocentric distance, stellar age, as well as reddening effects along the line of sight. Nonetheless, the results are tantalizing and appear in agreement with previous studies of SMC debris. As a consistency check, we applied our procedure to subsamples of LMC giants lying in the northeast and southwest regions of the disk. Given the viewing angles of the LMC, the northeast disk is lying at a closer heliocentric distance to us than the southwestern edge. Thus, this should be detectable in our method; indeed, we find a median magnitude offset of $-0.12$ mag for the giants located in the northeast and one of 0.03 mag for those in the southwest. These offset values are comparable to those of Li et al. (2016), who applied a similar method to M giants in the LMC.

### 4.4. Old Stellar Bridge

Given that we have found evidence for a population of stars within 8° of the SMC center, lying in front of the dwarf and displaying a kinematic signature of tidal disruption, a natural avenue of exploration is to now assess the stars lying directly in the inter-Cloud region as can be gleaned from Figure 17. Historically, the detection of a continuous path between the Clouds in intermediate and old stellar populations has proved elusive. Utilizing 2MASS and WISE photometry, Bagheri et al. (2013) selected a sample of giants, with ages ranging from ∼400 Myr to 5 Gyr in the bridge region, at low stellar density. The analysis of OGLE RGB and RC stars by Skowron et al. (2014) found little evidence of a coherent stellar bridge, but rather posited that the presence of evolved stellar populations in this region stems from the overlap of the MC's halos. They do however observe the diffuse structure of giants to lie predominantly south of the young bridge. This is consistent with the findings of Belokurov et al. (2017) who, on selecting RRL out of the Gaia DR1 catalog, were able to trace a continuous structure between the Clouds, offset by ∼5° south of the young MB. They argued this offset was formed under the scenario that both the gas and old RRL were stripped coevally from the SMC. The stripped gas was accosted by the hot gas of the MW corona in the form of ram pressure, essentially pushing it back and forming the offset. The spectroscopic study of inter-Cloud RGs by Carrera et al. (2017) found the chemistry and kinematics of their intermediate aged sample to be consistent with that of a tidally stripped SMC population, adding weight to the notion that an older stellar bridge exists in some form. Subsequently, the deep DECam imaging of Mackey et al. (2018) and the highly pure giant sample of Belokurov & Erkal (2019) revealed the presence of a tangled mix of ancient stellar populations in the Old MB region confirming the earlier discovery of Belokurov et al. (2017).

In the top panel of Figure 20, we show the stellar density of our giants in MB coordinates, with the black dashed box indicating the selection of stars lying in the bridge region. In the panel below, we show the distribution of metallicity of these giants progressively through the bridge. On moving through the outer LMC disk, the metallicity shows a steady decline, with the SMC profile remaining relatively flat out to $X_{\rm MB} \sim -15°$, just beyond which appears to lie a metal-poor sample of stars with [Fe/H] $\sim 1.5$ dex. Moving through the region of $-15° < X_{\rm MB} < -10°$, the metallicity structure becomes more complex and difficult to discern owing to the low stellar density in this region. Interestingly, however, there does appear to be a continuous ridge of constant metallicity, $\sim -1$ dex, running through this region, connecting the outer edge of the LMC out toward $X_{\rm MB} \sim -15°$. It is noteworthy that the metallicity along this ridge is consistent with the mean value of SMC giant's lying within the inner 4° of the dwarf, as well as that of the outer regions of the LMC. The lower two panels of the figure trace the proper motions through the bridge region, with $\mu_{Y_{\rm MB}}$ showing a relatively coherent structure that smoothly links the motions of the SMC to the LMC. The motion in $\mu_{X_{\rm MB}}$ is less well defined through the bridge region, with greater scatter about the general trend. This is consistent with the high level of dispersion we see in the lower-left panel

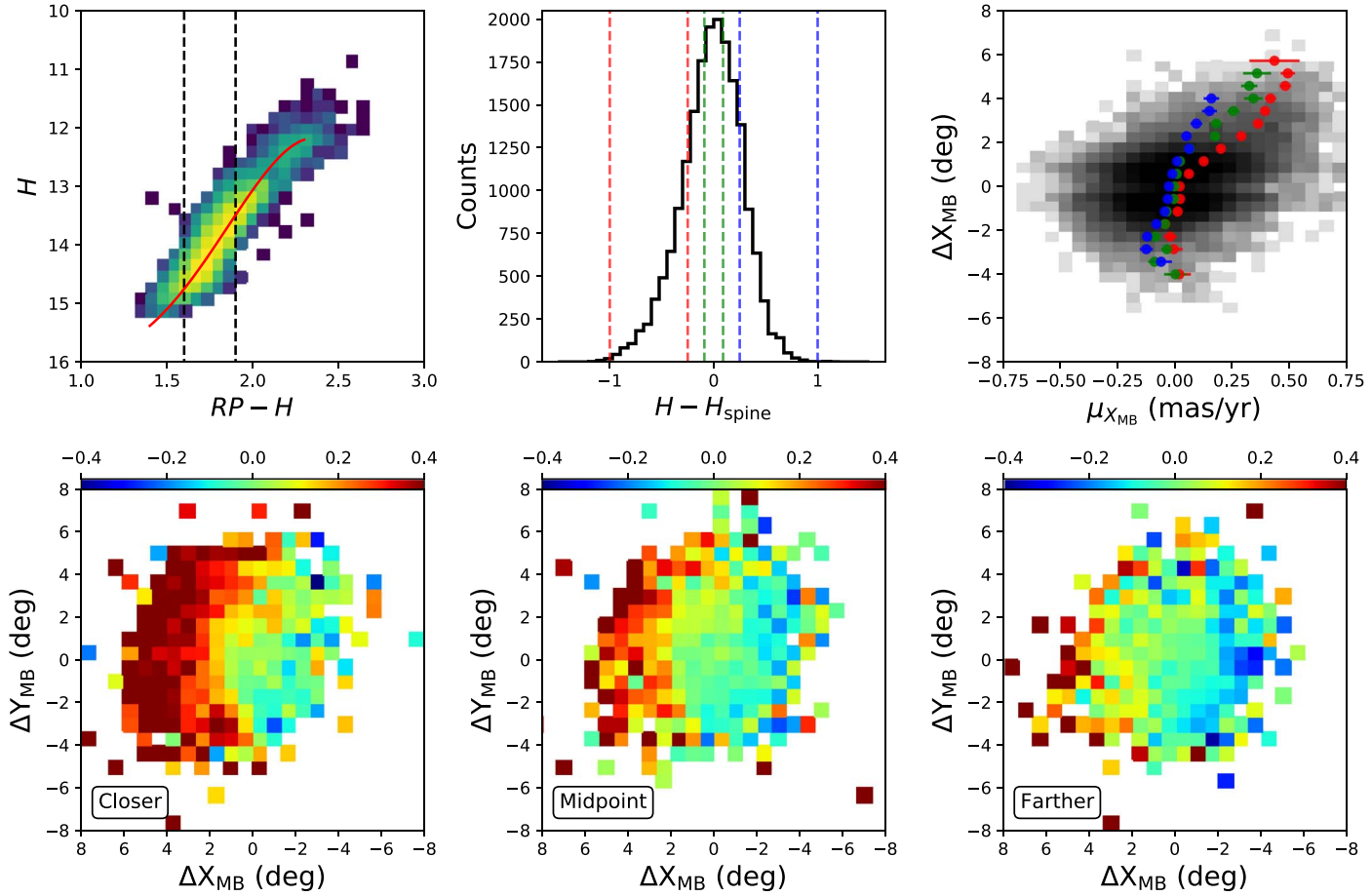


**Figure 19.** Upper left: CMD of SMC giants within a fixed metallicity range of $-1 < [\mathrm{Fe/H}] < -0.9$ dex. The solid red line shows the polynomial fitted to the RGB in this bin, offsets from which are taken as a proxy for heliocentric distance. As described in the text, we have fitted such polynomials to SMC giants lying in the range $-1.2 < [\mathrm{Fe/H}] < -0.5$ dex, over metallicity bins of width 0.1 dex. In computing the magnitude offset of our giants, we only consider those falling between the black dashed lines in the panel. Upper middle: we show the distribution of the magnitude offset of the SMC giants we select to analyze. The distribution is centered about zero and appears to be relatively symmetric about its peak, with a slight tail to negative values with these stars likely lying in front of the dwarf. Three bins in this distance proxy were selected to study the behavior of giants lying in front of, coincident with, and behind the center of the SMC. The boundaries of these bins are shown by the red, green, and blue dashed lines, respectively. Upper right: grayscale pixels show the logarithmic density of stars in their relative offset from the SMC center as a function of their motion in $\mu_{X_{\mathrm{MB}}}$. There is a distinct population of stars with excessive motion in $\mu_{X_{\mathrm{MB}}}$ along increasing $\Delta X_{\mathrm{MB}}$, toward the LMC. The scatter points are colored by their respective distances and show mean proper motion values as a function of $\Delta X_{\mathrm{MB}}$. We see that it is those giants lying predominantly in front of the SMC who exhibit such perturbed motion. This sequence becomes distinct in its behavior very centrally and rapidly evolves out to high values of $\mu_{X_{\mathrm{MB}}}$ with increasing angular distance away from the SMC core. Error bars represent the standard error weighted by the Poisson noise in each bin. Lower panels: we show the SMC giants in the three distance bins, with the closest in the left panel and the most distant in the right. Pixel colors correspond to mean values of $\mu_{X_{\mathrm{MB}}}$. This view of the SMC reinforces the result of the upper-right panel, where we can clearly see the giants lying closer to us being those most heavily disrupted in the direction of the LMC.

of Figure 15 at the interface of the two Clouds, as well as our results from Section 4.3. The signature of a flow of stars through the bridge region is consistent with the findings of Zivick et al. (2019) whose proper motion analysis of RGs through the bridge closely resembles our findings (see their Figure 8). The relatively complex metallicity distribution in the inter-Cloud region, alongside the high dispersion in $\mu_{X_{\mathrm{MB}}}$, renders it difficult to exactly discern the origin of the stars lying in this region. Further to this, the MB region is composed of giants tending toward the metal-poor end of our sample where our regression predictions are inherently more uncertain, owing to the lack of APOGEE training data in this regime, as gleaned from Figure 6. This adds to the difficulty in drawing firm conclusions on the metallicity distribution through the MB. It is, however, highly likely that the population of stars in this region is a mixture of both LMC and SMC giants. The origin of LMC debris in the bridge could be attributed to the effect of MW tides acting on the larger dwarf, with the *N*-body simulation of Belokurov et al. (2017) and Belokurov & Erkal (2019) demonstrating that such an effect can quite easily strip LMC debris to align well with the old stellar bridge.

In Figure 21, we show the sample of Gaia DR2 RRL described in Section 2 for which we are afforded heliocentric distance estimates. The left panel of the figure shows the Clouds in MB coordinates with pixels colored by mean heliocentric distance, where we see RRL lying at distances consistent with both the LMC and SMC in the old stellar bridge. Selecting RRL in the slice of $-10^{\circ} < Y_{\mathrm{MB}} < 0^{\circ}$, we show the distance distribution of these stars along $X_{\mathrm{MB}}$, revealing three interesting structures that pervade through the bridge region. First, two distinct filaments peel away from the LMC's western edge, one sits at ∼50 kpc, while the other some 5 kpc farther away. The closer RRL sequence stretching from the LMC meets halfway with the trailing tail of the SMC, emanating from the near end of the dwarf in the direction of the LMC. This appears to be consistent with our findings in

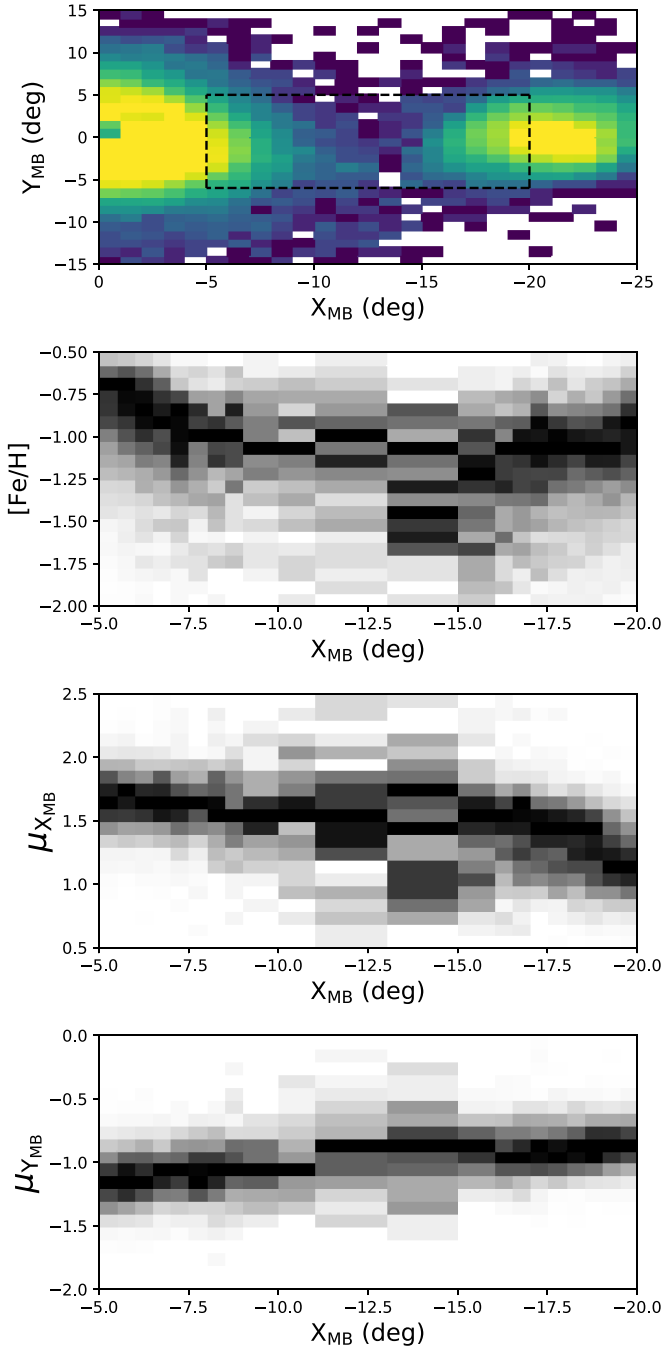


**Figure 20.** The top panels show the logarithmic density of giants in Magellanic Bridge coordinates. In the region between the Clouds, there exists a population of stars whose nature we would like to probe. On selecting stars falling within the black rectangle, we show their metallicity along the bridge in the panel below. The column-normalized density shows the evolution of giant metallicity upon the passage from the SMC to the LMC. Between the Clouds, it appears as if they are joined by a constant ridge at $\sim -1$ dex, a value consistent with both the outer regions of the LMC and the median value of all SMC giants. On moving outwards from the SMC, there appear to be two sequences: the ridge that connects to the LMC and a metal-poorer population that extends out to $X_{MB} \sim -13°$. The lower two panels show the proper motions of the stars through the bridge region, with a relatively smooth transition between the Clouds being apparent. The motion along $\mu_{X_{MB}}$ shows a degree of dispersion that is consistent with Figure 15.

Section 4.3, where we saw evidence for (likely unbound) giants lying in front of the SMC being kinematically disrupted toward the larger Cloud. The interpretation of the nature of the second (more distant) part of the bifurcated structure attached to the LMC at $\sim$55 kpc is more challenging. Are these LMC stars that have been stripped toward the SMC or vice versa? In the right panel, we show a column-normalized version of this representation. The distance gradient as mapped by the RRL appears to run almost uninterrupted from the east side of the LMC to the far side of the SMC. This is akin to the findings of Wagner-Kaiser & Sarajedini (2017) who observed a smooth transition in the distances of OGLE RRL between the Clouds. In this view of the line-of-sight distance distribution, the bifurcation on the LMC side of the old bridge is even more evident (also see the 1D slice shown in the inset). While the exact nature of the old bridge is still unclear, it appears from the RRL that both Clouds are joined by a population of stars over heliocentric distance, whose nature is likely dual, with debris having been stripped from both galaxies. The metallicity distribution of our giants between the Clouds supports this notion; giants with a wide range of metallicities appear to inhabit this region with two main structures apparent. We observe a metal-poor continuation of the outer SMC, appearing to extend out to $X_{MB} \sim -15°$, consistent with the SMC RRL we observe peeling away from the dwarf's trailing tail. Second to this is the ridge of $\sim -1$ dex that looks to span far into the bridge region, where from the RRL we see such LMC debris exists. We have seen the proper motion distribution of the giants to be turbulent through the bridge region, as stars from both Clouds are being stripped and thrust toward each other in a complex way.

## 5. Conclusions

We have amassed a sample of Magellanic RGs, drawn from Gaia DR2, demonstrating the ability to predict accurate photometric metallicities for such stars utilizing machine-learning methods. In doing so, we have produced some of the highest resolution metallicity maps of the Clouds to date. Utilizing our metallicity predictions in conjunction with the proper motions of our giants, we produced a chemo-kinematical mapping of the Magellanic system, which shows it to be fraught with intricacy as a consequence of its severe disruption.

We observe negative metallicity gradients on moving outwards through both Clouds. In modeling the LMC as a thin inclined disk, we infer a metallicity gradient of $-0.048 \pm 0.01$ dex kpc$^{-1}$, a value in good agreement with other estimates in the literature (see, e.g., Cioni 2009; Choudhury et al. 2016). Centrally, the profiles flatten as this region becomes dominated by the metal-rich bars. Various asymmetries are present in the metallicity profiles when considering different regions of each galaxy. Such features are readily visible in the LMC, where we observe the stellar bar, main spiral arm, and diffuse regions of metallicity enhancement in the disk. The most striking example is perhaps the southern spiral arm feature seen in the inner regions, a metal-rich component appearing to emanate from the western end of the bar and wrapping clockwise through the LMC disk. Spatially, this spiral-like feature is coincident with the stellar overdensity observed by Choi et al. (2018a), and it is very likely that historic LMC–SMC interactions have given rise to this intermediate aged stellar structure. We further observe a northern arc-like region of relative metal enhancement, coincident with the stellar feature observed by Besla et al. (2016) in their optical images of the LMC periphery. In their simulations of the Magellanic system, they concluded it is the repeated close encounters with the SMC that primarily seeds

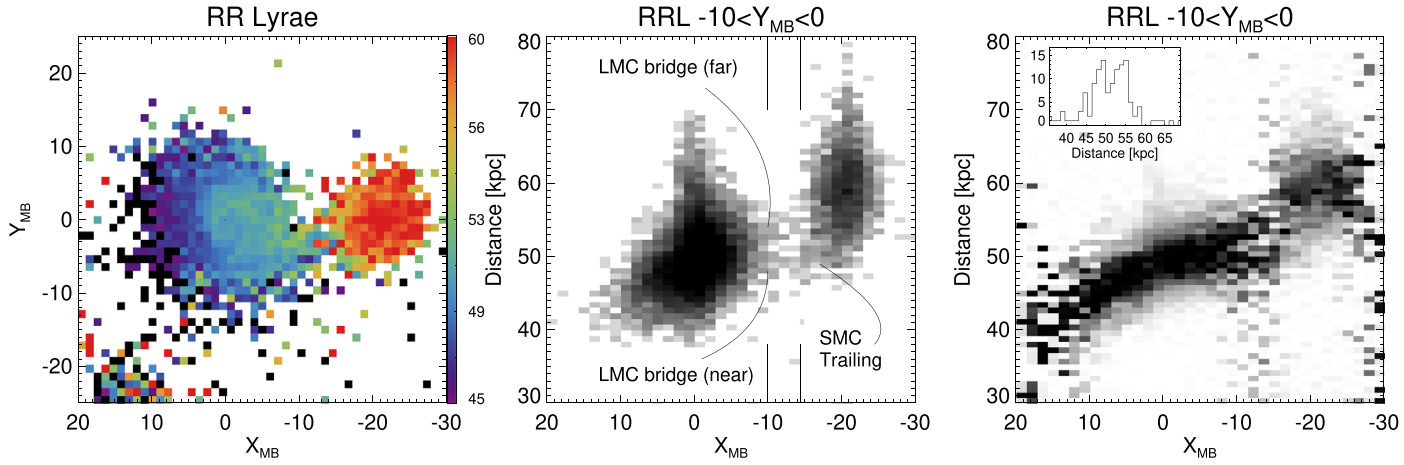


**Figure 21.** We show the Gaia DR2 RR Lyrae whose selection was described in Section 2. Left: pixels are colored by mean RRL heliocentric distance. A gradient is observed across the face of the LMC disk owing to its inclination. We also see RRL residing in the eastern portion of the SMC to lie at closer heliocentric distances. Between the Clouds, we see the old stellar bridge with stars lying at distances consistent with both Clouds. Middle: RRL distance is shown along $X_{\rm MB}$ for stars lying in the slice of $-10^{\circ} < Y_{\rm MB} < 0^{\circ}$. The SMC morphology is cigar-like, stretching along our line of sight. There appear to be two distinct structures lying between the Clouds at heliocentric distances of ∼50 and ∼55 kpc. The inset panel shows the distance distribution for RRL lying in the slice $-14^{\circ} < X_{\rm MB} < -10^{\circ}$ in which we observe a bimodality, with the two peaks associated with the dual structures stretching between the Clouds.

such one-sided stellar structures in the northern portion of the LMC, with the tidal field of the SMC alone able to induce one-armed spirals within the larger Cloud.

On slicing the Clouds by metallicity, we observe global evolution in the morphology of the two galaxies. Naturally, the majority of the outer substructure is observed in the more metal-poor giants, with those that are metal richer residing much more centrally in both instances. The outer northern and southern thin spiral-like arms in the LMC are again observed to rotate with the Cloud, lagging in their orbits, as was first noted by Belokurov & Erkal (2019). The metal-poor SMC giants located nearest to the LMC are hot in their motions, with high dispersion observed at the interface between the two dwarfs, a region where we naturally expect a mixture of stars originating from both the LMC and SMC. Further to this, in Figure 15, we observe the eastern portion of the SMC to bear increased motion in the direction of its larger counterpart. On studying the isodensity contours of the SMC, we observe them to display the S-shape signature characteristic of tidal disruption, a feature that appears to persist at all metallicities. We probe the SMC disruption further through a simple consideration of the proper motions of our giants. Utilizing each star's relative position in the CMD as a proxy for heliocentric distance, we ascertain that it is those giants likely lying closer to us that exhibit such fervent motion toward the larger Cloud. Our interpretation is that we are observing a tidal tail trailing the SMC, projected along our line of sight, that has been stripped away from the dwarf's core by the LMC. We trace this disruption down to the inner ∼2°–3° of the SMC, consistent with the foreground red clump population observed by Subramanian et al. (2017), which they tracked down to the inner ∼2 kpc (see Nidever et al. 2013 also). In essence, this stripped population constitutes the start of the old stellar bridge emanating away from the SMC toward the LMC. We do not observe any leading counterpart, and it may simply be that we do not possess enough distant giants in our sample to do so, as such debris is expected to lie ∼20 kpc directly behind the SMC (Diaz & Bekki 2012).

Finally, we consider giants lying in between the Clouds in the MB region. We, for the first time, trace the metallicity distribution through the region and find its nature to be dual; we observe a metal-poor component of [Fe/H] $\sim -1.5$ dex lying just beyond the eastern edge of the SMC, with a continuous metallicity ridge of approximately $-1$ dex appearing to span much of the distance between the two Clouds. We further consider the Gaia DR2 RRL around this region, with the added benefit that we can easily estimate the heliocentric distances for such stars. Two thin appendages appear to link the Clouds, lying at distances of ∼50 and 55 kpc. The SMC morphology appears cigar-like, with stellar debris appearing to emanate from the near-end of the dwarf, warping toward the LMC. It also appears that a population of LMC stars extends into the bridge region, indicating that the old stellar populations inhabiting the bridge are a mixture of stripped stars from both the LMC and the SMC.

J.G. thanks the Science and Technology Facilities Council of the United Kingdom for financial support.

## Data Availability

We provide the sample of 226,119 giants described in Section 2 hosted at doi:10.5281/zenodo.4077356. The catalog contains Gaia's `source_id`, photometry, and proper motion measurements alongside 2MASS and WISE photometry. We provide extinction values corrected in the manner explained in Section 2, as well as our metallicity predictions with associated errors according to Table 1.

## References

Bagheri, G., Cioni, M. R. L., & Napiwotzki, R. 2013, A&A, 551, A78
Belokurov, V., Erkal, D., Deason, A. J., et al. 2017, MNRAS, 466, 4711
Belokurov, V. A., & Erkal, D. 2019, MNRAS, 482, L9
Berentzen, I., Athanassoula, E., Heller, C. H., & Fricke, K. J. 2003, MNRAS, 341, 343
Besla, G., Kallivayalil, N., Hernquist, L., et al. 2007, ApJ, 668, 949
Besla, G., Kallivayalil, N., Hernquist, L., et al. 2012, MNRAS, 421, 2109
Besla, G., Martínez-Delgado, D., van der Marel, R. P., et al. 2016, ApJ, 825, 20
Bica, E., Bonatto, C., Dutra, C. M., & Santos, J. F. C. 2008, MNRAS, 389, 678
Carrera, R., Conn, B. C., Noël, N. E. D., Read, J. I., & López Sánchez, Á. R. 2017, MNRAS, 471, 4571
Carrera, R., Gallart, C., Aparicio, A., et al. 2008, AJ, 136, 1039

Casetti-Dinescu, D. I., Vieira, K., Girard, T. M., & van Altena, W. F. 2012, ApJ, 753, 123
Casey, A. R., Kennedy, G. M., Hartle, T. R., & Schlaufman, K. C. 2018, MNRAS, 478, 2812
Choi, Y., Nidever, D. L., Olsen, K., et al. 2018a, ApJ, 869, 125
Choi, Y., Nidever, D. L., Olsen, K., et al. 2018b, ApJ, 866, 90
Choudhury, S., de Grijs, R., Rubele, S., et al. 2020, MNRAS, 497, 3746
Choudhury, S., Subramaniam, A., & Cole, A. A. 2016, MNRAS, 455, 1855
Cignoni, M., Sabbi, E., & van der Marel, R. P. 2015, ApJ, 811, 76
Cioni, M. R. L. 2009, A&A, 506, 1137
Clementini, G., Ripepi, V., Molinaro, R., et al. 2019, A&A, 622, A60
Crowl, H. H., Sarajedini, A., Piatti, A. E., et al. 2001, AJ, 122, 220
Cullinane, L. R., Mackey, A. D., Da Costa, G. S., et al. 2020, MNRAS, 497, 3055
de Grijs, R., Wicker, J. E., & Bono, G. 2014, AJ, 147, 122
De Leo, M., Carrera, R., Noël, N. E. D., et al. 2020, MNRAS, 495, 98
De Marchi, G., Paresce, F., & Panagia, N. 2011, ApJ, 739, 27
de Vaucouleurs, G. 1955, AJ, 60, 126
de Vaucouleurs, G., & Freeman, K. C. 1972, VA, 14, 163
Deason, A. J., Belokurov, V., Erkal, D., Koposov, S. E., & Mackey, D. 2017, MNRAS, 467, 2636
Deb, S., Kurbah, K., Singh, H. P., et al. 2019, MNRAS, 489, 3725
Deb, S., Singh, H. P., Kumar, S., & Kanbur, S. M. 2015, MNRAS, 449, 2768
Diaz, J. D., & Bekki, K. 2012, ApJ, 750, 36
El Youssoufi, D., Cioni, M.-R. L., Bell, C. P. M., et al. 2019, MNRAS, 490, 1076
Foreman-Mackey, D., Hogg, D. W., Lang, D., & Goodman, J. 2013, PASP, 125, 306
Fraser-McKelvie, A., Merrifield, M., Aragón-Salamanca, A., et al. 2019, MNRAS, 488, L6
Gaia Collaboration, Babusiaux, C., van Leeuwen, F., et al. 2018a, A&A, 616, A10
Gaia Collaboration, Brown, A. G. A., Vallenari, A., et al. 2018b, A&A, 616, A1
Gaia Collaboration, Helmi, A., van Leeuwen, F., et al. 2018c, A&A, 616, A12
Gaia Collaboration, Prusti, T., de Bruijne, J. H. J., et al. 2016, A&A, 595, A1
Gardiner, L. T., & Hawkins, M. R. S. 1991, MNRAS, 251, 174
Haschke, R., Grebel, E. K., & Duffau, S. 2012, AJ, 144, 107
Hindman, J. V., Kerr, F. J., & McGee, R. X. 1963, AuJPh, 16, 570
Holl, B., Audard, M., Nienartowicz, K., et al. 2018, A&A, 618, A30
Indu, G., & Subramaniam, A. 2015, A&A, 573, A136
Iorio, G., & Belokurov, V. 2019, MNRAS, 482, 3868
Irwin, M. J. 1991, in IAU Symp. 148, The Magellanic Clouds, ed. R. Haynes & D. Milne (Cambridge: Cambridge Univ. Press), 453
Irwin, M. J., Demers, S., & Kunkel, W. E. 1990, AJ, 99, 191
Irwin, M. J., Kunkel, W. E., & Demers, S. 1985, Natur, 318, 160
Jacyszyn-Dobrzeniecka, A. M., Skowron, D. M., Mróz, P., et al. 2017, AcA, 67, 1
Kallivayalil, N., van der Marel, R. P., Besla, G., Anderson, J., & Alcock, C. 2013, ApJ, 764, 161
Koposov, S. E., Belokurov, V., Zucker, D. B., et al. 2015, MNRAS, 446, 3110
Li, J., Smith, M. C., Zhong, J., et al. 2016, ApJ, 823, 59
Mackey, A. D., Koposov, S. E., Da Costa, G. S., et al. 2017, MNRAS, 472, 2975
Mackey, A. D., Koposov, S. E., Erkal, D., et al. 2016, MNRAS, 459, 239
Mackey, D., Koposov, S., Da Costa, G., et al. 2018, ApJL, 858, L21
Majewski, S. R. & APOGEE Team & APOGEE-2 Team 2016, AN, 337, 863
Massana, P., Noël, N. E. D., Nidever, D. L., et al. 2020, MNRAS, 498, 1034
Moni Bidin, C., Casetti-Dinescu, D. I., & Girard, T. M. 2017, MNRAS, 466, 3077
Muraveva, T., Subramanian, S., Clementini, G., et al. 2018, MNRAS, 473, 3131
Nidever, D. L., Hasselquist, S., Hayes, C. R., et al. 2020, ApJ, 895, 88
Nidever, D. L., Majewski, S. R., & Butler Burton, W. 2008, ApJ, 679, 432
Nidever, D. L., Monachesi, A., Bell, E. F., et al. 2013, ApJ, 779, 145
Niederhofer, F., Cioni, M.-R. L., & Rubele, S. 2018, A&A, 613, L8
Nikolaev, S., Drake, A. J., Keller, S. C., et al. 2004, ApJ, 601, 260
Ochsendorf, B. B., Zinnecker, H., & Nayak, O. 2017, NatAs, 1, 784
Olsen, K. A. G., & Salyk, C. 2002, AJ, 124, 2045
Olsen, K. A. G., Zaritsky, D., Blum, R. D., Boyer, M. L., & Gordon, K. D. 2011, ApJ, 737, 29
Omkumar, A. O., Subramanian, S., Niederhofer, F., et al. 2021, MNRAS, 500, 2757
Pearson, S., Privon, G. C., Besla, G., et al. 2018, MNRAS, 480, 3069
Pedregosa, F., Varoquaux, G., Gramfort, A., et al. 2011, J. Mach. Learn. Res., 12, 2825
Piatti, A. E. 2018, MSRAS, 473, 4410
Ripepi, V., Cioni, M.-R.a L., & Moretti, M. I. 2017, MNRAS, 472, 808
Rubele, S., Girardi, L., Kerber, L., et al. 2015, MNRAS, 449, 639
Ruiz-Lara, T., Gallart, C., Monelli, M., et al. 2020, A&A, 639, L3
Salem, M., Besla, G., & Bryan, G. 2015, ApJ, 815, 77
Schlaufman, K. C., & Casey, A. R. 2014, ApJ, 797, 13
Schlegel, D. J., Finkbeiner, D. P., & Davis, M. 1998, ApJ, 500, 525
Schmidt, T., Cioni, M.-R. L., Niederhofer, F., et al. 2020, A&A, 641, A134
Scowcroft, V., Freedman, W. L., Madore, B. F., et al. 2016, ApJ, 816, 49
Seidel, M. K., Falcón-Barroso, J., Martínez-Valpuesta, I., et al. 2016, MNRAS, 460, 3784
Shapley, H. 1940, BHarO, 914, 8
Skowron, D. M., Jacyszyn, A. M., Udalski, A., et al. 2014, ApJ, 795, 108
Skowron, D. M., Skowron, J., Udalski, A., et al. 2021, ApJS, 252, 23
Skrutskie, M. F., Cutri, R. M., Stiening, R., et al. 2006, AJ, 131, 1163
Stanimirović, S., Staveley-Smith, L., & Jones, P. A. 2004, ApJ, 604, 176
Subramanian, S., Rubele, S., Sun, N.-C., et al. 2017, MNRAS, 467, 2980
Subramanian, S., & Subramaniam, A. 2012, ApJ, 744, 128
van de Ven, G., van den Bosch, R. C. E., Verolme, E. K., & de Zeeuw, P. T. 2006, A&A, 445, 513
van der Marel, R. P., & Cioni, M.-R. L. 2001, AJ, 122, 1807
van der Marel, R. P., & Kallivayalil, N. 2014, ApJ, 781, 121
van Gelder, M. L., Kaper, L., & Japelj, J. 2020, A&A, 636, A54
Wagner-Kaiser, R., & Sarajedini, A. 2017, MSRAS, 466, 4138
Walker, I. R., Mihos, J. C., & Hernquist, L. 1996, ApJ, 460, 121
Wright, E. L., Eisenhardt, P. R. M., Mainzer, A. K., et al. 2010, AJ, 140, 1868
Yuan, H. B., Liu, X. W., & Xiang, M. S. 2013, MNRAS, 430, 2188
Zaritsky, D., Harris, J., Grebel, E. K., & Thompson, I. B. 2000, ApJL, 534, L53
Zasowski, G., Cohen, R. E., Chojnowski, S. D., et al. 2017, AJ, 154, 198
Zhao, H., & Evans, N. W. 2000, ApJL, 545, L35
Zivick, P., Kallivayalil, N., Besla, G., et al. 2019, ApJ, 874, 78
Zivick, P., Kallivayalil, N., van der Marel, R. P., et al. 2018, ApJ, 864, 55